

Where Are the Baryons? III: Non-Equilibrium Effects and Observables

Renyue Cen¹ and Taotao Fang²

Received _____; accepted _____

arXiv:astro-ph/0601009v1 31 Dec 2005

¹Princeton University Observatory, Princeton, NJ 08544; cen@astro.princeton.edu

²Department of Astronomy, University of California, Berkeley, CA 94720; fangt@astro.berkeley.edu; *Chandra Fellow*

ABSTRACT

Numerical simulations of the intergalactic medium have shown that at the present epoch a significant fraction (40 – 50%) of the baryonic component should be found in the ($T \sim 10^6\text{K}$) Warm-Hot Intergalactic Medium (WHIM) - with several recent observational lines of evidence indicating the validity of the prediction. We here recompute the evolution of the WHIM with the following major improvements: (1) galactic superwind feedback processes from galaxy/star formation are explicitly included; (2) major metal species (O V to O IX) are computed explicitly in a non-Equilibrium way; (3) mass and spatial dynamic ranges are larger by a factor of 8 and 2, respectively, than in our previous simulations. We find: (1) non-equilibrium calculations produce significantly different results from ionization equilibrium calculations. (2) The abundance of O VI absorption lines based on non-equilibrium simulations with galactic superwinds is in remarkably good agreement with latest observations, implying the validity of our model, while the predicted abundances for O VII and O VIII absorption lines appear to be lower than observed but the observational errorbars are currently very large. The expected abundances for O VI (as well as Ly α), O VII and O VIII absorption systems are in the range 50 – 100 per unit redshift at $EW = 1\text{km/s}$ decreasing to 10 – 20 per unit redshift at $EW = 10\text{km/s}$. The number of O VI absorption lines with $EW > 100\text{km/s}$ is very small, while there are about 1 – 3 lines per unit redshift for O VII and O VIII absorption lines at $EW = 100\text{km/s}$. (3) Emission lines, primarily O VI and Ly α in the UV and O VII and O VIII in the soft X-rays are potentially observable by future missions and they provide complimentary probes of the WHIM in often different domains of the temperature-density-metallicity phase space as well as in different spatial locations; however, sometimes they overlap spatially and in phase space, making

joint analyses very useful. The number of emission lines per unit redshift that may be detectable by planned UV and soft X-ray missions are in the order of 0.1 – 1.

Subject headings: Cosmology: observations, large-scale structure of Universe, intergalactic medium

1. Introduction

Cosmological hydrodynamic simulations have strongly suggested that most of the previously “missing” baryons may be in a gaseous phase in the temperature range $10^5 - 10^7$ K and at moderate overdensity (Cen & Ostriker 1999, hereafter ”CO”; Davé 2001), called the warm-hot intergalactic medium (WHIM), with the primary heating process being hydrodynamic shocks from the formation of large-scale structure at scales currently becoming nonlinear. The reality of the WHIM has now been quite convincingly confirmed by a number of observations from HST, FUSE, Chandra and XMM-Newton (Tripp, Savage, & Jenkins 2000; Tripp & Savage 2000; Oegerle et al. 2000; Scharf et al. 2000; Tittley & Henriksen 2001; Savage et al. 2002; Fang et al. 2002; Nicastro et al. 2002; Mathur, Weinberg, & Chen 2002; Kaastra et al. 2003; Finoguenov, Briel, & Henry 2003; Sembach et al. 2004; Nicastro et al. 2005).

In addition to shock heating, feedback processes following star formation in galaxies can heat gas to the same WHIM temperature range. What is lacking theoretically is a satisfactory understanding of the known feedback processes on the WHIM and how the WHIM may be used to understand and calibrate the feedback processes. Another unsettled issue is how the predicted results will change if one has a more accurate, non-equilibrium calculation of the major metal species, such as O VI, O VII and O VIII, since time scales for ionization and recombination are not widely separated from the Hubble time scale. In a companion paper (Cen & Ostriker 2005) we have studied the effects of galactic superwinds on the IGM, and in particular on WHIM. Additional improvements include significantly larger dynamic ranges of the simulation, a WMAP normalized cosmological model and an improved radiative transfer treatment. The purpose of this paper is to present additional effects due to non-equilibrium calculations on major observable metal species, such as O VI, O VII and O VIII. Our current work significantly extends previous theoretical works by

our group and others (CO; Davé 2001; Cen et al. 2001; Fang et al. 2002; Chen et al. 2003; Furlanetto et al. 2004,2005a,b; Yoshikawa et al. 2003; Ohashi et al. 2004; Suto et al. 2004; Fang *et al.* 2005). The outline of this paper is as follows: the simulation details are given in §2; in §3 we give detailed results and discussion and conclusions are presented in §4.

2. Simulations

The reader should refer to Cen & Ostriker (2005) for a detailed description of the computation method. Here we will only briefly explain the basic hydrodynamic code, explain the cosmological model that we use, the simulation box parameters and relevant treatment details on how major oxygen species are computed.

The results reported on here are based on new simulations of a *WMAP*-normalized (Spergel et al. 2003; Tegmark et al. 2004) cold dark matter model with a cosmological constant, $\Omega_M = 0.31$, $\Omega_b = 0.048$, $\Omega_\Lambda = 0.69$, $\sigma_8 = 0.89$, $H_0 = 100h\text{kms}^{-1}\text{Mpc}^{-1} = 69\text{kms}^{-1}\text{Mpc}^{-1}$ and $n = 0.97$. The adopted box size is $85\text{Mpc}/h$ comoving and with a number of cells of 1024^3 , the cell size is $83\text{kpc}/h$ comoving, with dark matter particle mass equal to $3.9 \times 10^8 h^{-1} M_\odot$. Given a lower bound of the temperature for almost all the gas in the simulation ($T \sim 10^4$ K), the Jeans mass $\sim 10^{10} M_\odot$ for mean density gas, which is comfortably larger than our mass resolution.

As described in Cen & Ostriker (2005), we have made simulations with and without galactic superwinds (GSW). Metals are produced self-consistently from star formation by adopting a specific efficiency of metal formation, a “yield” (Arnett 1996), $y_0 = 0.02$, the percentage of stellar mass that is ejected back into IGM as metals for Type II supernovae (SNe II), which we follow accurately in the simulation. On the other hand, accurately following the evolution of metal ejection (approximately half of the iron) from Type I

supernovae (SNe I) is difficult in large part due to the uncertainties in theoretical modeling of SNe I. Since oxygen is predominantly produced by SNe II, our results on oxygen related quantities are very insensitive to the lack of treatment of SNe I. Metals produced by SNe II are followed as a separate variable (analogous to the total gas density) with the same hydrocode. In addition, we implement another density variable to keep track of the reprocessed, i.e., secondary metals in the ejecta (such as S process elements), which is proportional to the metallicity of the gas from which the star was formed. There are two adjustable parameters with regard to overall metal production, namely, y_0 from SNe II and y_I from SNe I in terms of metal contribution. These two parameters are uncertain theoretically but may be normalized by observed oxygen and iron abundances in ICM. The oxygen and iron abundance is ~ 0.5 and ~ 0.3 solar in the ICM of observed clusters (e.g., Mushotzky et al. 1996; Tamura et al. 2004) and there is indication that there is about an equal amount of contribution to the iron mass in ICM from SNe Ia and SNe II (e.g., Etori 2005). Following Tsujimoto et al. (1995), using metal yield patterns for SNe Ia and SNe II with Salpeter IMF, we find that in order to match the observed iron metallicity of ~ 0.3 solar in ICM, we need a SNe II metal yield $y_0 = 0.03$ instead of the value 0.02 adopted, taking into account that one half of the iron in ICM would have been contributed by SNe Ia. However, this still leaves us with an oxygen abundance in the computed ICM of ~ 0.25 solar (using $y_0 = 0.03$) versus the observed value of ~ 0.5 solar (Mushotzky et al. 1996; Tamura et al. 2004). This deficit in oxygen mass in ICM can not be made up by SNe Ia in any reasonable abundance, because they do not produce a significant amount of oxygen mass. We do not yet know the actual solution to this problem. Possible solutions may include an IMF that is significant flatter than the adopted Salpeter IMF, which would produce more SNe II and more hypernovae, which are prime producers of oxygen. Alternatively, one may increase the star formation efficiency by some factor, say, ~ 2 , to bring oxygen abundance into better agreement with observations, which would then require

some adjustment on the contribution to iron mass in ICM from SNe Ia. This is a very complex issue and there may be hints that a simple combination of SNe II and SNe Ia with the standard IMF may not be adequate (e.g., Dupke & White 2000; Portinari et al. 2004; Baumgartner et al. 2005), and it is beyond the scope of this paper to attempt to address this issue. What we must do, however, is to normalize the simulated abundances of both iron and oxygen to the observed values in ICM as closely as we can. This requirement translates to an enhancement of oxygen abundance by a factor of $\sim 3 = 0.03/0.02 \times 2$, where the factor $0.03/0.02$ is needed to normalize to ICM iron abundance (see Figure 15 below) and the factor 2 is to further normalize to ICM oxygen abundance; we stress again that the underlying cause for the factor 2 is unclear at present. Aside from this unknown scaling factor, oxygen is known to be predominantly produced by SNe II and hence the computed spatial and temporal evolution of oxygen distribution should remain accurate; we simply multiply the oxygen abundance at every spatial point in the simulation by a factor of 3. Once this re-normalization procedure is done, we have no further freedom to make any other adjustment with regard to metallicity, specifically, oxygen abundances, in any other regions of the IGM, which are the focus of this study. We have adopted a solar oxygen abundance of 8.78 dex, which is close to but about 20% higher than recently determined values (Allende Prieto, Lambert, & Asplund 2001; Asplund et al. 2004).

The implementation of the major oxygen species is done as follows. We follow the evolution of O IV to O IX simultaneously by directly integrating five rate equations for each cell in a non-equilibrium fashion. Each oxygen species is followed as a separate variable and each conservation equation (without the source terms) is solved using the same TVD hydrodynamics code, taking into account recombination (Shull & van Steenberg 1982), collisional ionization (Aldrovandi & Pequignot 1973; Shull & van Steenberg 1982; Arnaud & Rothenflug 1985; Arnaud & Raymond 1992; Verner & Ferland 1996; Voronov 1997) and photoionization (Clark, Cowan, & Bobrowicz 1986; Verner et al. 1996) processes for

a non-uniform cosmological density field. Relevant coefficients for these processes and equations are enclosed in the Appendix for completeness.

3. Results

We present and compare simulations with and without galactic superwinds (GSW; Cen & Ostriker 2005) and between calculations that assume ionization-equilibrium and detailed non-equilibrium calculations.

3.1. Metal Absorption Lines in UV and X-ray

We present detailed results on major absorption lines, including O VI ($\lambda\lambda 1032, 1038$), O VII ($\lambda 21.6$) and O VIII ($\lambda 19.0$). The detailed evolution of all these major metal species is followed in a non-equilibrium fashion, by solving rate equations for each cell at each timestep explicitly. The evolution also depends on the detailed background radiation field as a function of redshift, which we compute in a self-consistent way in our simulations taking into account both sources and sink computed directly in simulations, shown in Figure 1. All our results presented below are at $z \sim 0$ and hence the $z=0$ radiation field is used when we compute metal abundances for some species based on CLOUDY (equilibrium) method. We note that the computed $z = 0$ radiation field is consistent with observations (Shull et al. 1999) and so is the radiation field at higher redshifts (Rauch et al. 1997; Bolton et al. 2005) and with observationally derived evolution of the background radiation field (Haardt & Madau 1999).

Figure 2 shows the number of O VI absorption lines per unit redshift as a function of equivalent width from simulations with and without GSW, from the case based on the simulation using CLOUDY program based on the simulation with GSW, all compared to

observations (symbols). First, we note that the simulation with appropriate GSW and non-equilibrium calculation (solid curve) is in excellent agreement with direct observations (symbols). This is quite remarkable considering that we have not attempted to make any fine-tuning on model parameters and the only two major parameters that have significant effects are e_{GSW} and y , where the latter is normalized to observed X-ray cluster gas abundance and the former is chosen to match the observed galactic superwinds (e.g., Pettini et al. 2002). In other words, our model is basically free of adjustable parameters other than overall yield and e_{GSW} and it is fair to say that the excellent agreement between our calculation and observations is a strong indication that our cosmological model is a faithful representation of the true universe in this regard.

However, the excellent agreement would not have been found, had the GSW effect not been included (dotted curve) or if we had adopted the equilibrium (CLOUDY) treatment is performed (dashed curve). Both GSW feedback and non-equilibrium method produce significant errors for abundances of low equivalent widths absorption lines ($EW \leq 30\text{\AA}$). Fortuitously, one may obtain an apparently reasonable agreement between theoretical calculations and observations if both errors in modeling are simultaneously made, i.e., an equilibrium CLOUDY treatment on a simulation with no significant GSW feedback; this is a mere coincidence. The physical reason why the equilibrium treatment produced more O VI than non-equilibrium simulation is that collisional ionization time scales are longer than the time scale on which gas is shock heated, especially for low density regions; for the very high density regions, the two approaches should agree, as Figure 2 indicates. Results obtained here are broadly consistent with with earlier simulations (Cen et al. 2001; Fang & Bryan 2001; Chen et al. 2003) and with analytic work (Furlanetto et al. 2005b) with regard to O VI absorption line abundance, taking into account various uncertainties about cosmological model parameters, different treatments of metallicity and assumptions about ionization equilibrium.

Figure 3 shows the number of O VII absorption lines per unit redshift as a function of equivalent width from simulations with (solid curve) and without (dotted curve) GSW. Also included as a dashed curve is what one would obtain using CLOUDY program based on the simulation with GSW. Somewhat different from the case for O VI, we see here that the feedback and non-equilibrium effects each produce a 30 – 50% change in the opposite direction in the predicted number of O VII absorption lines for the entire range of width. Figure 4 is similar to Figure 3 but for O VIII absorption lines and comparable effects due to GSW and equilibrium treatment are seen. In both cases for O VII and O VIII absorption lines the agreement between observations and our detailed non-equilibrium calculations with GSW are not as good as that for the O VI absorption line see in Figure 2. However, the observational errorbars for the abundances of these two absorption lines are currently very large due to a very small observational sample. The physical reason behind the results that the equilibrium treatment produced more O VII and O VIII than non-equilibrium simulation is similar to that given for the case of O VI, except that the collisional ionization time scales are still longer in the case of O VII and O VIII and the times scales on which gas is shock heated are still shorter than for O VI. as Figure 2 indicates. It will be of great importance to enlarge observational samples for both O VII and O VIII absorption lines to make more statistically sound comparisons. Since our model has no adjustable parameters except yield and e_{GSW} , the outcome from such comparisons will provide critical tests of yield, e_{GSW} and the underlying cosmological model.

To summarize the relative abundances of these major species, Figure 5 displays results for all three absorption lines in terms of equivalent widths in units of km/s to indicate the relative abundances of the three major species. The conversion between EW in $m\text{\AA}$ and EW in km/s is: $EW(m\text{\AA}) = \lambda EW(km/s)/c$, which is equal to $(34.3m\text{\AA})(EW(km/s)/10km/s)$, $(0.35m\text{\AA})(EW(km/s)/50km/s)$ and $(0.32m\text{\AA})(EW(km/s)/50km/s)$, for O VI, O VII and O VIII, respectively. The expected abundances for these three lines are in the range 50 – 100

per unit redshift at $EW = 1\text{km/s}$ decreasing to 10 – 20 per unit redshift at $EW = 10\text{km/s}$; the rate of decrease of the line abundance at higher EW then becomes significantly higher. The number of O VI absorption lines with $EW > 100\text{km/s}$ is very small, while there are about 1 – 3 lines per unit redshift for O VII and O VIII absorption lines at $EW = 100\text{km/s}$. The computed O VII and O VIII absorption line abundances are in reasonable agreement with Chen et al. (2003), in particular, for their “scatter” metallicity model (dashed curve in Figure 7 of Chen et al. 2003), considering large uncertainties on metallicity distribution and ionization equilibrium assumption.

Figure 6 shows the average metallicity (with scatter) of O VI, O VII and O VIII absorption lines as a function of equivalent widths. We see two clear trends, albeit with significant scatter: (1) at low EW on average O VI absorption lines have lowest metallicity, while O VIII absorption lines have highest metallicity. (2) for each absorption line higher EW lines have higher metallicity. Overall, on average, O VI lines have a metallicity range of $0.15 - 0.60 Z_{\odot}$ with a large scatter at the low end. The O VII absorption lines have a mean metallicity range $0.20 - 0.60 Z_{\odot}$ with a somewhat larger scatter at the low end than the O VI line. The O VIII absorption lines, quite interestingly, display a nearly constant mean metallicity of $\sim 0.5 - 0.6 Z_{\odot}$ over the entire EW range. All three absorption lines converge to a mean metallicity of $0.6 Z_{\odot}$ at the high EW end with a scatter of about $0.2 Z_{\odot}$. These figures, (19)-(24), present one of the two primary observational predictions of this paper.

Figure 7 shows the Doppler width b as a function of equivalent width EW for O VI, O VII and O VIII, from top to bottom panel. We see that the Doppler widths for the three species all have a concentration broadly in the range of 10 – 60 km/s at the low EW end. This suggests that peculiar velocity effect plays a very important role here. It should be noted that peculiar velocities affects widths in complex ways, either broadening or narrowing, depending on detailed velocity and shock structures. In some cases, Hubble

expansion could counter the effect of peculiar velocities of enclosing double shocks. Most of the very low b structures are likely photo-ionized and overall velocity broadening effect is minimal. On the high EW end, the trend is somewhat more clear. There, values of b of O VI, O VII and O VIII appear to increase more or less monotonically in that order. This is due to the fact that higher ionization species are closer to center of potential wells, thus have, on average, higher temperatures and velocities.

Finally, Figures 8,9,10 show in detail three randomly chosen lines of sight through the simulation boxes that have significant absorption features. Noticeable features in these figures are: (1) GSW in most cases tend to broaden the absorption line profiles. (2) GSW may alter absorption profile in complex ways as clearly seen in the bottom two panels of Figure 8 for O VII and O VIII lines, caused by a combination of separate effects on the gas velocity, temperature, metallicity and density. (3) The typical gas density of the absorption features seen is in the range of 10 – 300 times the mean gas density. (4) The typical metallicity of gas producing the prominent UV absorption lines is in the range $0.1 - 1.0 Z_{\odot}$. (5) The significant absorption features are usually enclosed by double shocks with velocity in the range 100 – 400km/s, i.e., we are seeing the outer edges of a cooling “Zeldovich pancake”. In fact, such pattern has been detected in a cluster of multiphase absorbers along the sightline toward PKS 2155-304 (Shull *et al.* 2003). We note that multiphase medium, while common, most often does not spatially co-exist; rather, complex velocity, density, and metallicity structure mask their appearances when observed in Hubble space. (6) The Doppler line widths for deep lines have 100 – 300km/s, while for more abundant small lines the widths are small, in the range of 1 – 100km/s. (7) The relative absorption strengths of the three considered lines vary and no particular order is visible, as expected, since the line strengths are functions of several physical variables. More detailed studies will be deferred to a subsequent paper.

3.2. Emission Lines in UV and X-ray

In order to map out directly the WHIM structure in 3 dimensions, detailed emission measurements are invaluable, because of their potential for continuous coverage and a lack of a dependence on the sparsely distributed background sources as required for absorption studies. We will focus on three metal emission lines, O VI, O VII and O VIII as well as the Ly α emission line. Emission tables were generated using a software package called CHIANTI (<http://www.solar.nrl.navy.mil/chianti.html>), based on electron density and density of a specific metal species.

Figure 11 shows the cumulative number of O VI and Ly α lines in UV per unit redshift as a function of surface brightness. The red curves show results from the simulation with GSW and the green curve from the simulation without GSW. The black curve (for O VI line only) is computed using CLOUDY code on the assumption of ionization equilibrium based on the density, temperature and metallicity information from the simulation with GSW. The results found with regard to Ly α emission may be compared to Figure 8 of Furlanetto et al. (2005a). Their figure has a different units for the ordinate, while the abscissa has the same units. In order to convert the values of the ordinates in their Figure 8 to dn/dz displayed here, we need to multiply their value in the vertical axis by $(dl/dz)/\delta l = 4478$, where $\delta l = 0.67h^{-1}\text{Mpc}$ is their pixel depth and $dl/dz = 3000h^{-1}\text{Mpc}$ is the length per unit redshift at $z = 0$. Good agreements are found between their results and ours. For example, at surface brightness of $\phi = 10^2 \text{ photons cm}^{-2} \text{ s}^{-1} \text{ sr}^{-1}$, we find $dn/dz(> \phi) = 0.33$ (thin solid curve in Figure 11), while their values range from 0.11 (panel b of their Figure 8) to 0.70 (panels a and c of their Figure 8). Also, we may compare the results found with regard to O VI emission to Figure 9 of Furlanetto et al. (2004), which shows the PDF (defined as $dn/d \ln \phi$ for $\delta z = 0.01$) of O VI emission. Integrating, for example, the dotted curve in panel (c) of their Figure 9, we find their $dn/dz(> \phi) = 0.40$ at surface brightness of $\phi = 10^2$

photons $\text{cm}^{-2} \text{s}^{-1} \text{sr}^{-1}$, which should be compared to our value of 0.61 (thick solid curve in Figure 11). At face value, their emission estimate is somewhat lower than ours but the difference should be considered to be small, given many physical and numerical factors involved. Therefore, we instead consider this a good agreement.

Figure 12 shows a similar plot for O VII and O VIII lines in soft X-rays. Note that future planned UV missions (for O VI and Ly α lines) may be able to achieve a sensitivity in the range 100 – 1000 in the displayed units and the proposed soft X-ray missions (for O VII and O VIII lines; DIOS – Yoshikawa et al. 2003; MBE – Fang et al. 2005) is expected to be able to achieve a sensitivity of order 0.1 in the displayed units for a reasonable amount of exposure time. We see that both UV emission lines such as Ly α , O VI and soft X-ray emission lines such as O VII and O VIII have comparable abundance. The number of emission lines per unit redshift that may be detectable by planned UV and soft X-ray missions are in the order of 0.1 – 1. Therefore, it is highly desirable to be able to map out emission in both UV and X-ray bands, because they often probe complimentary physical regions.

How large a fraction of the baryons may be probed by these metal emission lines? Figures 13,14 show the total amount of baryons that can be probed by emission lines as a function of the surface brightness. For the quoted sensitivities in the range 100 – 1000 in the displayed units, we see that O VI line may be able to probe about 0.5 – 1.5% of all baryons or 1 – 3% of WHIM, while the Ly α emission line may be able to probe about 4 – 6% of WHIM. The DIOS and MBE X-ray mission is expected to be able to detect 10% and 20% of WHIM, using O VII and O VIII lines, respectively, which may be compared to calculations by Yoshikawa et al. (2004b) who found that at $10^{-10} \text{ erg s}^{-1} \text{ cm}^{-2} \text{ sr}^{-1}$ (which corresponds to our adopted DIOS and MBE sensitivity of $\phi = 0.1 \text{ photons cm}^{-2} \text{ s}^{-1} \text{ sr}^{-1}$) the WHIM mass fractions probed O VII and O VIII are 18% and 20%, respectively. Given

the difference in the treatments between ours and theirs the agreement is to be considered good and this also suggest that the local universe, as they simulated, represents a fair sample of the universe with regard to WHIM. Since metal enrichment of the IGM is quite inhomogeneous, these emission lines, being in overdense regions, should be able to track a larger fraction of metals produced in star formation. Figures 15,16 show that the O VI emission line will be able to probe about 1.5 – 4% of all metals in the IGM, while the O VII and O VIII emission lines will be able to probe about 15 – 30% of all metals in the IGM. In all the above figures (Figures 11-16) we show that GSW affect quantitative results dramatically; omission of GSW effect could cause errors 100 – 1000% with regard to line abundances, baryonic densities and metal densities.

Figures 17,18 show the observable regions in the sky (black regions) of a map of size $85 \times 85 \text{Mpc}^2/h^2$ using O VI and Ly α lines, respectively, with an instrument of a sensitivity of 100 photon $\text{cm}^{-2}\text{sr}^{-1}\text{s}^{-1}$. Figures 19,20 show the observable regions in the sky (black regions) of a map of size $85 \times 85 \text{Mpc}^2/h^2$ using O VII and O VIII lines, respectively, with an instrument of a sensitivity of 0.1 photon $\text{cm}^{-2}\text{sr}^{-1}\text{s}^{-1}$ (DIOS). The red contours are the underlying gas density distribution. It is quite clear that, while detectable regions by these UV and soft X-ray emission lines can not continuously cover the entire filamentary network, they provide a faithful representation of the underlying density structure, especially the filaments. It may be noted that O VI and Ly α lines provide rather poor tracer for some the of the larger red contour concentrations, because the latter are sites of hotter gas in the WHIM temperature range, too hot to be traceable by these UV emission lines; O VII and O VIII X-ray emission lines provide a relatively better set of probers for this hot gas. Figures 21,22,23,24 zoom in to a smaller region of Figure 17,18,19,20 respectively, to better display the detailed correspondence between detectable regions and the underlying density structure. We see that both O VI and Ly α lines tend to avoid the larger density knots and often appear to be off-centered, i.e., located in the outskirts of large density concentrations.

In contrast, the O VII and O VIII emission lines most often directly overlap with the larger density concentrations and do not probe the outskirts of them. This clearly illustrates the complementarity of UV and X-ray emission missions, dictated by the complex physical structure of the WHIM in the vicinity of galaxies and groups of galaxies. The physical variables that play important roles here are gas temperature, gas density, gas metallicity and gas peculiar velocity. None of these can be tracked simply but all of them are expected to be influenced significantly by GSW. Therefore, detailed comparisons between simulations and observations, when becoming available, may provide an extremely valuable tool to probe galaxy formation and its all important feedback processes.

4. Discussion and Conclusions

In Cen & Ostriker (2005) we show that our significantly improved simulations confirm previous conclusions based on earlier simulations: *nearly one half of all baryons at the present epoch should be found in the WHIM* - a filamentary network in the temperature range of $10^5 - 10^7$ K. There, we also presented significant effects due to feedback from star formation.

Here we investigate detailed ionization distributions of oxygen, computed explicitly in a non-Equilibrium way, and present results related to important UV and soft X-ray lines and how their observations may shed light on WHIM and galaxy formation processes. Our findings are: (1) non-equilibrium calculations produce significantly different results from equilibrium calculations, and the differences are complex and difficult to characterize simply. (2) The abundance of O VI absorption lines based on non-equilibrium simulations with galactic superwinds is in remarkably good agreement with latest observations, implying the validity of our model, while the predicted abundances for O VII and O VIII absorption lines appear to be lower than observed but the observational errorbars are currently very

large. The expected abundances for O VI (as well as Ly α), O VII and O VIII lines are in the range 50 – 100 per unit redshift at $EW = 1\text{km/s}$ decreasing to 10 – 20 per unit redshift at $EW = 10\text{km/s}$. The number of O VI absorption lines with $EW > 100\text{km/s}$ is very small, while there are about 1 – 3 lines per unit redshift for O VII and O VIII absorption lines at $EW = 100\text{km/s}$. (3) Emission lines, primarily O VI and Ly α in the UV and O VII and O VIII in the soft X-rays are potentially observable by future missions and they provide complimentary probes of the WHIM in often different domains in the temperature-density-metallicity phase space as well as in different spatial locations; however, sometimes they overlap spatially and in phase space, making joint analyses very useful. The number of emission lines per unit redshift that may be detectable by planned UV and soft X-ray missions are in the order of 0.1 – 1.

We expect that future missions in UV and X-ray should be able to provide much more accurate characterization of the WHIM through two complimentary approaches: major UV and soft X-ray absorption lines and emission lines. The former will be able to trace out bulk of the mass as well as volume occupied by the WHIM, whereas the latter will be able to probe higher density regions. Together they may allow us to construct a coherent picture of the evolution of the IGM. In addition, detailed useful information may be obtained by investigating relations between galaxies and properties of the WHIM, keeping in mind that GSW play an essential role exchanging mass, metals and energy between them. We stress that proper comparisons between observations and simulations in the vicinity of galaxies where GSW effects originate and are strongest may provide one of the most useful ways to probe star formation and its all important feedback processes.

We thank Ed Jenkins for kindly providing emission tables for oxygen species. We thank Ed Jenkins, Jerry Ostriker and Mike Shull for useful comments. The simulations were performed at the Pittsburgh Supercomputer Center. We thank R. Reddy at the Pittsburgh

Supercomputer Center for constant and helpful assistance in the process of making the simulations. This work is supported in part by grants NNG05GK10G and AST-0507521. T. Fang was supported by the NASA through *Chandra* Postdoctoral Fellowship Award Number PF3-40030 issued by the *Chandra* X-ray Observatory Center, which is operated by the Smithsonian Astrophysical Observatory for and on behalf of the NASA under contract NAS8-39073.

REFERENCES

- Aldrovandi, S. M. V., & Pequignot, D. 1973, *A&A*, 25, 137
- Allende Prieto, C., Lambert, D.L., & Asplund, M. 2001, *ApJ*, 556, L63
- Arnaud, M., & Raymond, J. 1992, *ApJ*, 398, 394
- Arnaud, K. A., et al. 1994, *ApJ*, 436, L67
- Arnaud, M., & Rothenflug, R. 1985, *A&AS*, 60, 425
- Asplund, M., Grevesse, N., Sauval, A.J., Allende Prieto, C., & Kiselman 2004, *A&A*, 417, 751
- Baumgartner, W.H., Loewenstein, M., Horner, D.J., Mushotzky, R.F. 2005, *ApJ*, 620, 680
- Bolton, J.S., Haehnelt, M.G., Viel, M., & Springel, V. 2005, *MNRAS*, 357, 1178
- Cen, R. 1992, *ApJS*, 78, 341
- Cen, R. 2003, *ApJ*, 591, 12
- Cen, R., & McDonald, P. 2002, *ApJ*, 570, 457
- Cen, R. & Ostriker, J. P. 1999, *ApJ*, 519, L109, “CO”.
- Cen, R., Nagamine, K., & Ostriker, J.P. 2005, *ApJ*, in press
- Cen, R. Tripp, T.M., Ostriker, J.P., & Jenkins, E.B. 2001, *ApJ*, 559, L5.
- Chen, X., Weinberg, D.H., Katz, N., & Davé, R. 2003, *ApJ*, 594, 42
- Clark, R. E. H., Cowan, R. D., & Bobrowicz, F. W. 1986, *Atomic Data and Nuclear Data Tables*, 34, 415

- Dupke, R.A., & Anaud, K.A. 2001, ApJ, 548, 141
- Dupke, R.A., & White, R.E., III 2000, ApJ, 537, 123
- Elizondo, D., Yepes, G., Kates, R., Muller, V., & Klypin, A. 1999a, ApJ, 515, 525
- Elizondo, D., Yepes, G., Kates, R., & Klypin, A. 1999b, NewA, 4, 101
- Ettori, S. 2005, MNRAS, 362, 110
- Fan, X., et al. 2002, AJ, 123, 1247
- Fang, T., Davis, D.S., Lee, J.C., Marshall, H.L., Bryan, G.L., & Canizares, C.R. 2002a, ApJ, 565, 86
- Fang, T., Marshall, H.L., Lee, J.C., Davis, D.S., & Canizares, C.R. 2002b, ApJ, 527, L127
- Fang, T., Sembach, K.R., & Canizares, C.R. 2003, ApJ, 586, L49
- Fang, T., Croft, R. A. C., Sanders, W. T., Houck, J., Davé, R., Katz, N., Weinberg, D. H., & Hernquist, L. 2005, ApJ, 623, 612
- Fang, T., & Bryan, G. L. 2001, ApJ, 564, L31
- Fang, T., Bryan, G. L., & Canizares, C. R. 2002, ApJ, 564, 604
- Ferland, G. J., Korista, K. T., Verner, D. A., Ferguson, J. W., Kingdon, J. B., & Verner, E. M. 1998, PASP, 110, 761
- Finoguenov, A., Briel, U.G., & Henry, J.P. 2003, A& A, 410, 777
- Fukugita, M., Hogan, C.J., & Peebles, P.J.E. 1998, ApJ, 503, 518
- Furlanetto, S.R., Schaye, J., Springel, V., & Hernquist, L. 2004, ApJ, 606, 221
- Furlanetto, S.R., Schaye, J., Springel, V., & Hernquist, L. 2005a, ApJ, 622, 7

- Furlanetto, S.R., Phillips, L.A., & Kamionkowski, M. 2005b, MNRAS, 359, 295
- Gnedin, N.Y., & Ostriker, J.P. 1997, ApJ, 486, 581
- Haardt, F., & Madau, P. 1999, ApJ, 514, 648
- Hultman, J., & Pharasyn, A. 1999, A&A, 347, 769
- Kaastra, J.S., Lieu, R., Tamura, T., Paerels, F.B.S., & den Herder, J.W. 2003, A& A, 397, 445
- Mathur, S., Weinberg, D.H., & Chen, X. 2003, ApJ, 582, 82
- Mushotzky, R. F., & Lowenstein, M. 1997, ApJ, 481, L63
- Mushotzky, R. F., Lowenstein, M., Arnaud, A. K., Tamura, T., Fukazawa, Y., Matsushita, K., Kikuchi, K., & Hatsukade, I. 1996, ApJ, 466, 686
- Nicastro, F., et al. 2005, Nature, 433, 495
- Oegerle, W.R., et al. 2000, ApJ, 538, L20
- Peebles, P.J.E. 1999, preprint, astro-ph/9910234
- Penton, S.V., Stocke, J.T., & Shull, J.M. 2004, ApJS, 152, 29
- Portinari, L., Moretti, A., Chiosi, C., & Sommer-Larsen, J. 2004, ApJ, 604, 579
- Rauch, M. et al. 1997, ApJ, 489, 7
- Ricotti, M., & Ostriker, J.P. 2004, MNRAS, 350, 539
- Ritchie, B. W., & Thomas, P. A. 2001, MNRAS, 323, 743
- Sembach, K.R., Tripp, T.M., Savage, B.D., & Richter, P. 2004, ApJS, 155, 351

- Savage, B.D., Sembach, K.R., Tripp, T.M., & Richter, P. 2002, ApJ, 564, 631
- Scharf, C., Donahue, M., Voit, G.M., Rosati, P., & Postman, M. 2000, ApJ, 528, L73
- Shull, J. M., Tumlinson, J., & Giroux, M. L. 2003, ApJ, 594, L107
- Shull, J. M., & van Steenberg, M. 1982, ApJS, 48, 95
- Shull, J. M., et al. 1999, AJ, 118, 1450
- Shapley, A.E., et al. 2005, in preparation.
- Springel, V., & Hernquist, L. 2003, MNRAS, 339, 289
- Steidel, C.C., Pettini, M., & Adelberger, K.L. 2001, ApJ, 546, 665
- Tamura, T., et al. 1996, PASP, 48, 671
- Tamura, T., et al. 2004, A&A, 420, 135
- Tegmark, M., et al. 2004, Phy. Rev. D, 69, 103501
- Tittley, E.R., & Henriksen, M.J. 2001, ApJ, 563, 673
- Tozzi, P., Rosati, P., Ettori, S., Borgani, S., Mainieri, V., & Norman, C. 2003, ApJ, 593, 705
- Tripp, T. M., Savage, B. D. & Jenkins, E. B. 2000, ApJ, 534, L1
- Tripp, T. M., & Savage, B. D. 2000, ApJ, 542, 42
- Tsujimoto, T., Nomoto, K., Yoshii, Y., Hashimoto, M., Yanagida, S., & Thielemann, F.-K. 1995, MNRAS, 277, 945
- Verner, D. A., & Ferland, G. J. 1996, ApJS, 103, 467

Verner, D. A., Ferland, G. J., Korista, K. T., & Yakovlev, D. G. 1996, *ApJ*, 465, 487

Voronov, G. S. 1997, *Atomic Data and Nuclear Data Tables*, 65, 1

Yepes, G., Kates, R., Khokhlov, A., & Klypin, A. 1997, *MNRAS*, 284, 235

Yoshikawa, K., et al. 2003, *PASJ*, 55, 879

Yoshikawa, K., et al. 2004b, *PASJ*, 56, 939

Yu, Q., & Tremaine, S. 2002, *MNRAS*, 335, 965

A. Equations for Non-Equilibrium Evolution of Oxygen Species

The ionization fractions of major oxygen species are calculated in a non-equilibrium evolution fashion. Specifically, we calculate the ionization fractions from O V to O IX by considering three major processes: (1) photoionization; (2) collisional ionization; and (3) recombination. If we define the ionization fraction of species i is X_i , the time-dependend evolution of X_i is determined by

$$\frac{dX_i}{dt} = -X_i\Gamma_i - \alpha_i X_i n_e - \beta_i X_i n_e + X_{i-1}\Gamma_{i-1} + \alpha_{i+1} X_{i+1} n_e + \beta_{i-1} X_{i-1} n_e. \quad (\text{A1})$$

Here Γ is the photoionization rate of, given by

$$\Gamma = \int_{\nu_0}^{\infty} \frac{4\pi J_\nu}{h\nu} \sigma(\nu) d\nu, \quad (\text{A2})$$

where ν_0 is the ionization frequency, J_ν is the background radiation, and σ is the photoionization cross section, which we adopted from Verner et al. (1996). Here n_e is the electron density, α is the recombination rate adopted from Shull & Steenberg (1982), and β

is the collisional ionization rate adopted from Voronov (1997). We solve the combined set of equations for species O I to O IV using a first-order implicit scheme, necessary for the stiff equations considered here. Given a time step of Δt , the ion number density at step $N + 1$ are determined by the following set of equations:

$$\begin{aligned}
 n_{\text{O V}}^{N+1} &= n_{\text{O V}}^N - (n_{\text{O V}}^{N+1} n_e^N \beta_{\text{O V}} + n_{\text{O V}}^{N+1} \Gamma_{\text{O V}}) \Delta t \\
 &\quad + n_{\text{O VI}}^{N+1} n_e^N \alpha_{\text{O V}} \Delta t \\
 n_{\text{O VI}}^{N+1} &= n_{\text{O VI}}^N - (n_{\text{O VI}}^{N+1} n_e^N \beta_{\text{O VI}} + n_{\text{O VI}}^{N+1} n_e^N \alpha_{\text{O V}} + n_{\text{O VI}}^{N+1} \Gamma_{\text{O VI}}) \Delta t \\
 &\quad + (n_{\text{O V}}^{N+1} n_e^N \beta_{\text{O V}} + n_{\text{O VII}}^{N+1} n_e^N \alpha_{\text{O V}} + n_{\text{O V}}^{N+1} \Gamma_{\text{O V}}) \Delta t \\
 n_{\text{O VII}}^{N+1} &= n_{\text{O VII}}^N - (n_{\text{O VII}}^{N+1} n_e^N \beta_{\text{O VII}} + n_{\text{O VII}}^{N+1} n_e^N \alpha_{\text{O VI}} + n_{\text{O VII}}^{N+1} \Gamma_{\text{O VII}}) \Delta t \\
 &\quad + (n_{\text{O VI}}^{N+1} n_e^N \beta_{\text{O VI}} + n_{\text{O VIII}}^{N+1} n_e^N \alpha_{\text{O VI}} + n_{\text{O VI}}^{N+1} \Gamma_{\text{O VI}}) \Delta t \\
 n_{\text{O VIII}}^{N+1} &= n_{\text{O VIII}}^N - (n_{\text{O VIII}}^{N+1} n_e^N \beta_{\text{O VIII}} + n_{\text{O VIII}}^{N+1} n_e^N \alpha_{\text{O VII}} + n_{\text{O VIII}}^{N+1} \Gamma_{\text{O VIII}}) \Delta t \\
 &\quad + (n_{\text{O VII}}^{N+1} n_e^N \beta_{\text{O VII}} + n_{\text{O IX}}^{N+1} n_e^N \alpha_{\text{O VII}} + n_{\text{O VII}}^{N+1} \Gamma_{\text{O VII}}) \Delta t
 \end{aligned} \tag{A3}$$

the above set of the equations is completed by

$$n_{\text{O IX}} = n_{\text{O}} - (n_{\text{O V}} + n_{\text{O VI}} + n_{\text{O VII}} + n_{\text{O VIII}}). \tag{A4}$$

To simplify notations, we define

$$x \equiv n_{\text{O V}} ; y \equiv n_{\text{O VI}} ; z \equiv n_{\text{O VII}} ; w \equiv n_{\text{O VIII}} , \tag{A5}$$

and the final solution to Eq.(A3) is then

$$\begin{aligned}
 x^{N+1} &= b^7 x^N + b^8 y^N + b^9 z^N + b^{10} w^N + b^{10} a^{11} n_{\text{O}} \\
 y^{N+1} &= \left(b^1 b^7 - \frac{1}{a^2}\right) + b^1 b^8 y^N + b^1 b^9 z^N + b^1 b^{10} w^N + b^1 b^{10} a^{11} n_{\text{O}} \\
 z^{N+1} &= (b^2 b^7 - b^3) + \left(b^2 b^8 - \frac{1}{a^5}\right) y^N + b^2 b^9 z^N + b^2 b^{10} w^N + b^2 b^{10} a^{11} n_{\text{O}} \\
 w^{N+1} &= (b^4 b^7 + b^5) + (b^4 b^8 - b^6) y^N + \left(b^4 b^9 - \frac{1}{a^8}\right) z^N + b^4 b^{10} w^N + b^4 b^{10} a^{11} n_{\text{O}}
 \end{aligned} \tag{A6}$$

Here we define:

$$\begin{aligned}
 a^1 &\equiv n_e^N \beta_{\text{O V}} \Delta t; & a^2 &\equiv n_e^N \alpha_{\text{O V}} \Delta t; & a^3 &\equiv \Gamma_{\text{O V}} \Delta t \\
 a^4 &\equiv n_e^N \beta_{\text{O VI}} \Delta t; & a^5 &\equiv n_e^N \alpha_{\text{O VI}} \Delta t; & a^6 &\equiv \Gamma_{\text{O VI}} \Delta t \\
 a^7 &\equiv n_e^N \beta_{\text{O VII}} \Delta t; & a^8 &\equiv n_e^N \alpha_{\text{O VII}} \Delta t; & a^9 &\equiv \Gamma_{\text{O VII}} \Delta t \\
 a^{10} &\equiv n_e^N \beta_{\text{O VIII}} \Delta t; & a^{11} &\equiv n_e^N \alpha_{\text{O VIII}} \Delta t; & a^{12} &\equiv \Gamma_{\text{O VIII}} \Delta t
 \end{aligned} \tag{A7}$$

and

$$\begin{aligned}
 b^1 &\equiv (1 + a^1 + a^3)(a^2)^{-1} \\
 b^2 &\equiv [(1 + a^1 + a^3)(1 + a^2 + a^4 + a^6) - (a^1 + a^3)a^2] (a^2 a^5)^{-1} \\
 b^3 &\equiv (1 + a^2 + a^4 + a^6)(a^2 a^5)^{-1} \\
 b^4 &\equiv [(1 + a^5 + a^7 + a^9)b^2 - (a^4 + a^6)b^1] (a^8)^{-1} \\
 b^5 &\equiv [(a^4 + a^6) - (1 + a^5 + a^7 + a^9)a^2 b^3] (a^2 a^8)^{-1} \\
 b^6 &\equiv (1 + a^5 + a^7 + a^9)(a^5 a^8) \\
 b^7 &\equiv [a^{11}/a^2 - (a^7 + a^9 - a^{11})b^3 - (1 + a^8 + a^{10} + a^{11} + a^{12})b^5] \\
 &\quad [(1 + a^8 + a^{10} + a^{11} + a^{12})b^4 + a^{11} + a^{11}b^1 - (a^7 + a^9 - a^{11})b^2]^{-1} \\
 b^8 &\equiv [(1 + a^8 + a^{10} + a^{11} + a^{12})b^6 - (a^7 + a^9 - a^{11})/a^5] \\
 &\quad [(1 + a^8 + a^{10} + a^{11} + a^{12})b^4 + a^{11} + a^{11}b^1 - (a^7 + a^9 - a^{11})b^2]^{-1} \\
 b^9 &\equiv [(1 + a^8 + a^{10} + a^{11} + a^{12})/a^8] \\
 &\quad [(1 + a^8 + a^{10} + a^{11} + a^{12})b^4 + a^{11} + a^{11}b^1 - (a^7 + a^9 - a^{11})b^2]^{-1} \\
 b^{10} &\equiv [(1 + a^8 + a^{10} + a^{11} + a^{12})b^4 + a^{11} + a^{11}b^1 - (a^7 + a^9 - a^{11})b^2]^{-1}
 \end{aligned} \tag{A8}$$

We test our equations by comparing calculations against ionization fractions obtained from various literatures and/or output from CLOUDY (Ferland et al. 1998), based on three cases: (1) collisional ionization only; (2) including additional photonization with a background radiation field of $J(912\text{\AA}) = 10^{-22} \text{ ergs s}^{-1} \text{ cm}^{-2} \text{ Hz}^{-1} \text{ sr}^{-1}$; and (3) photonization with a background radiation field of $J(912\text{\AA}) = 10^{-23} \text{ ergs s}^{-1} \text{ cm}^{-2} \text{ Hz}^{-1} \text{ sr}^{-1}$. Here $J(912\text{\AA})$ is the specific flux at 912 Å, and we adopt a power law spectrum with a spectral index of -1 . To make the comparison to available equilibrium calculations, we run our simulations

long enough so eventually all the ion species are in ionization equilibrium. Figure 25 shows the comparison for the collisional ionization case with zero background radiation field. The solid lines in each panel are results from our calculation, and the diamonds are adopted from Mazzotta et al. (1998). Except O V, all the other ion species show excellent agreements between our calculations and those from Mazzotta et al. (1998), which are calculated based on collisional ionization equilibrium. Figures 26 and 27 show the comparison for case (2) and (3), respectively. The symbols are the same as those in Figure 25. These comparisons clearly demonstrate that our simulation reproduces the ionization fractions under a variety of possible cases that have bearing on our actual calculations.

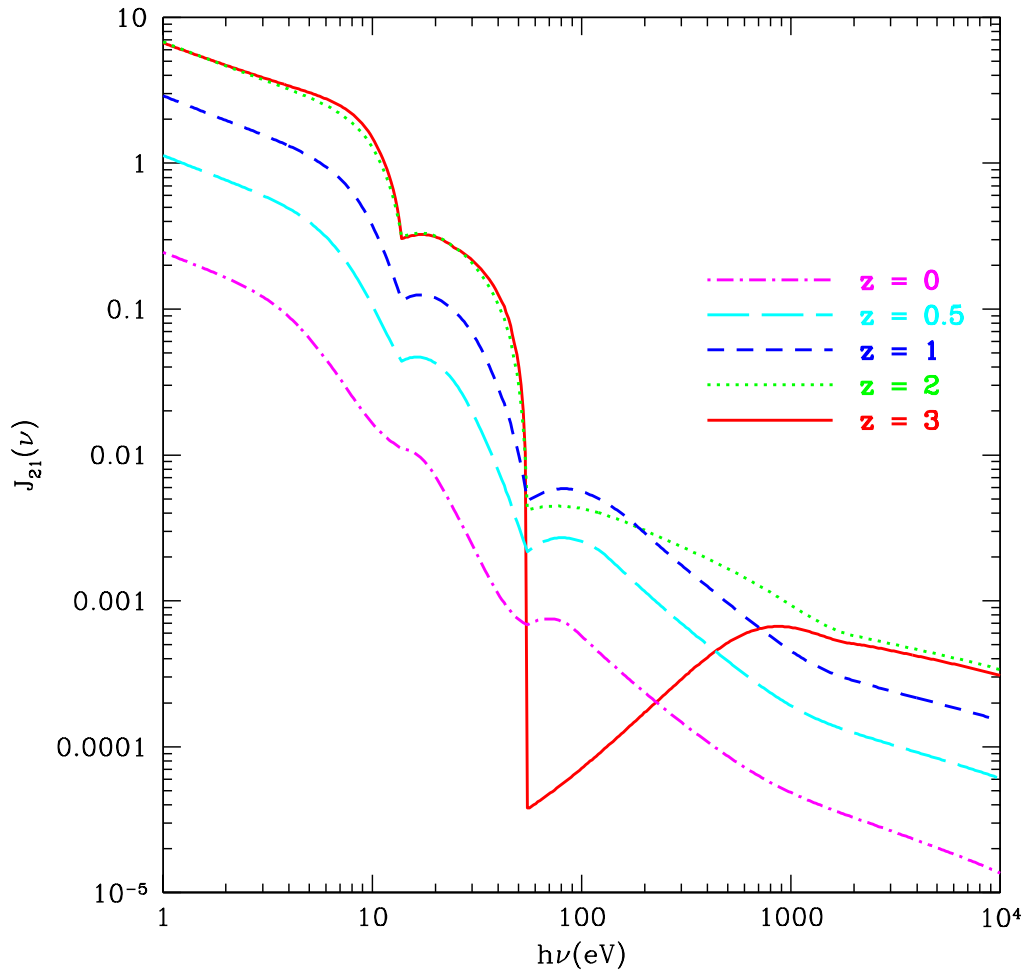


Fig. 1.— shows the background radiation field in units of $10^{-21}\text{erg}/\text{cm}^2/\text{sec}/\text{sr}$, at five redshift, $z=3,2,1,0.5,0$, computed in our simulations.

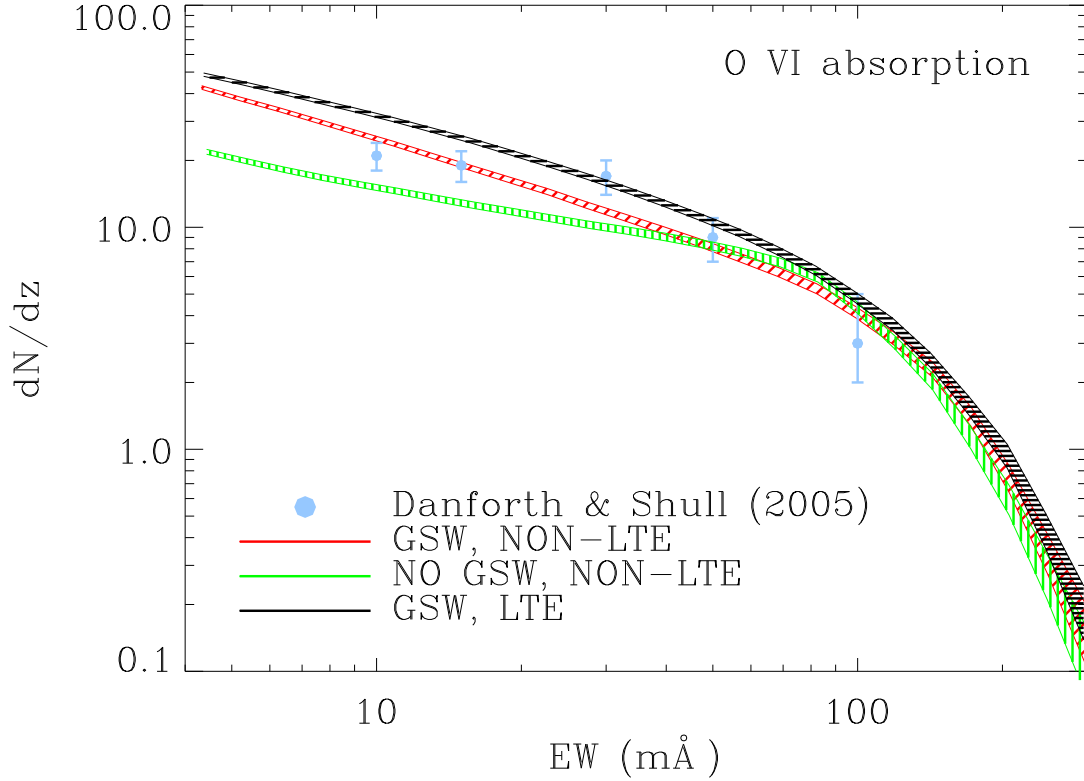


Fig. 2.— shows the number of O VI absorption lines per unit redshift as a function of equivalent width in units of $\text{m}\text{\AA}$. The red curve shows our primary results from the simulation with GSW and the green curve from the simulation without GSW. The black curve is computed using CLOUDY code on the assumption of ionization equilibrium based on the density, temperature and metallicity information from the simulation with GSW. The symbols are observations by Danforth & Shull (2005).

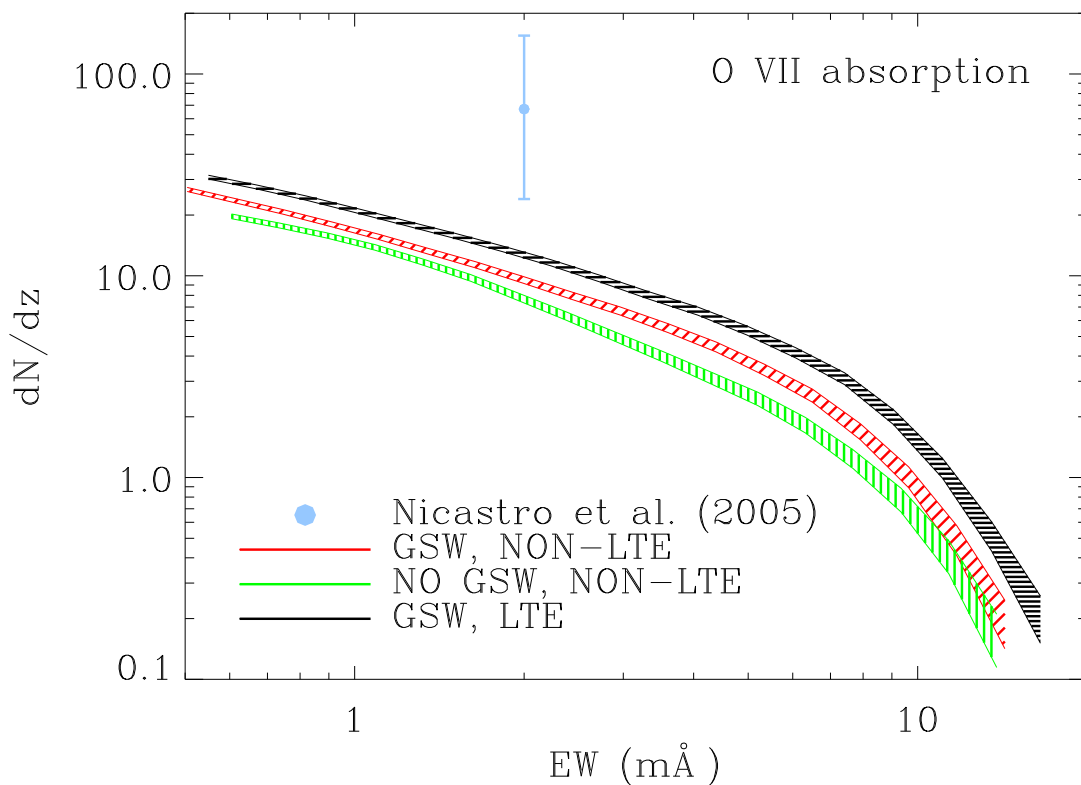


Fig. 3.— shows the number of O VII absorption lines per unit redshift as a function of equivalent width in units of mÅ. The red curve shows results from the simulation with GSW and the green curve from the simulation without GSW. The black curve is computed using CLOUDY code on the assumption of ionization equilibrium based on the density, temperature and metallicity information from the simulation with GSW. The symbols are observations by Nicastro et al. (2005).

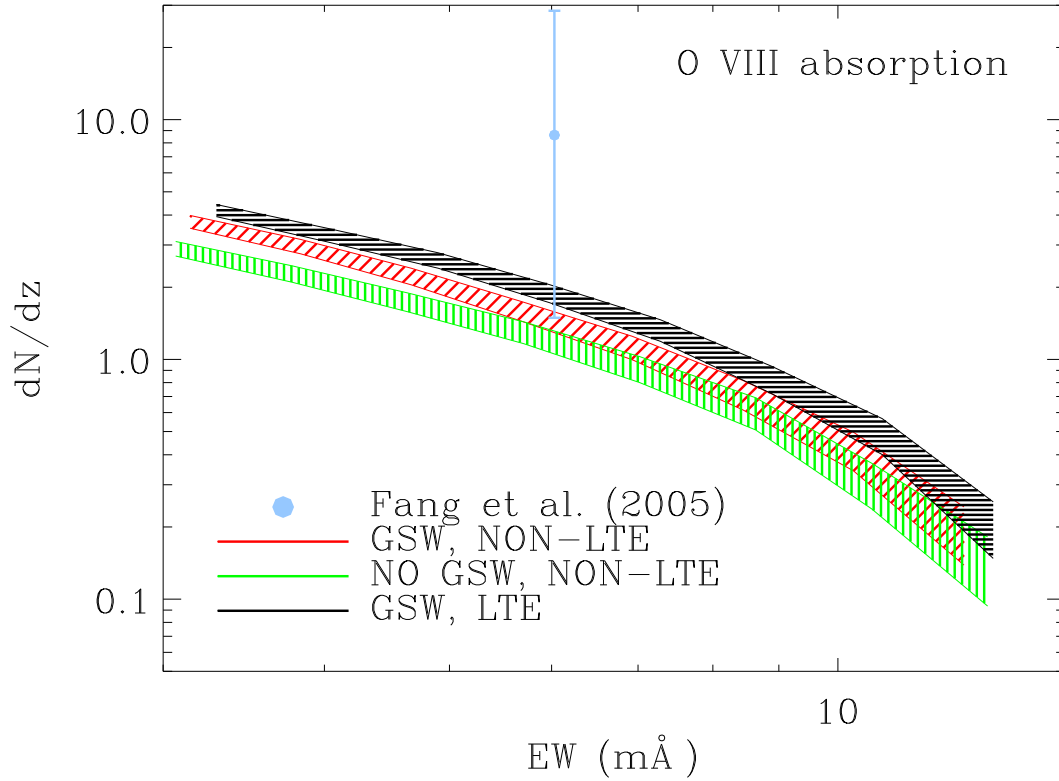


Fig. 4.— shows the number of O VIII lines per unit redshift as a function of equivalent width. The red curve shows results from the simulation with GSW and the green curve from the simulation without GSW. The black curve is computed using CLOUDY code on the assumption of ionization equilibrium based on the density, temperature and metallicity information from the simulation with GSW. The symbols are observations by Fang et al. (2005).

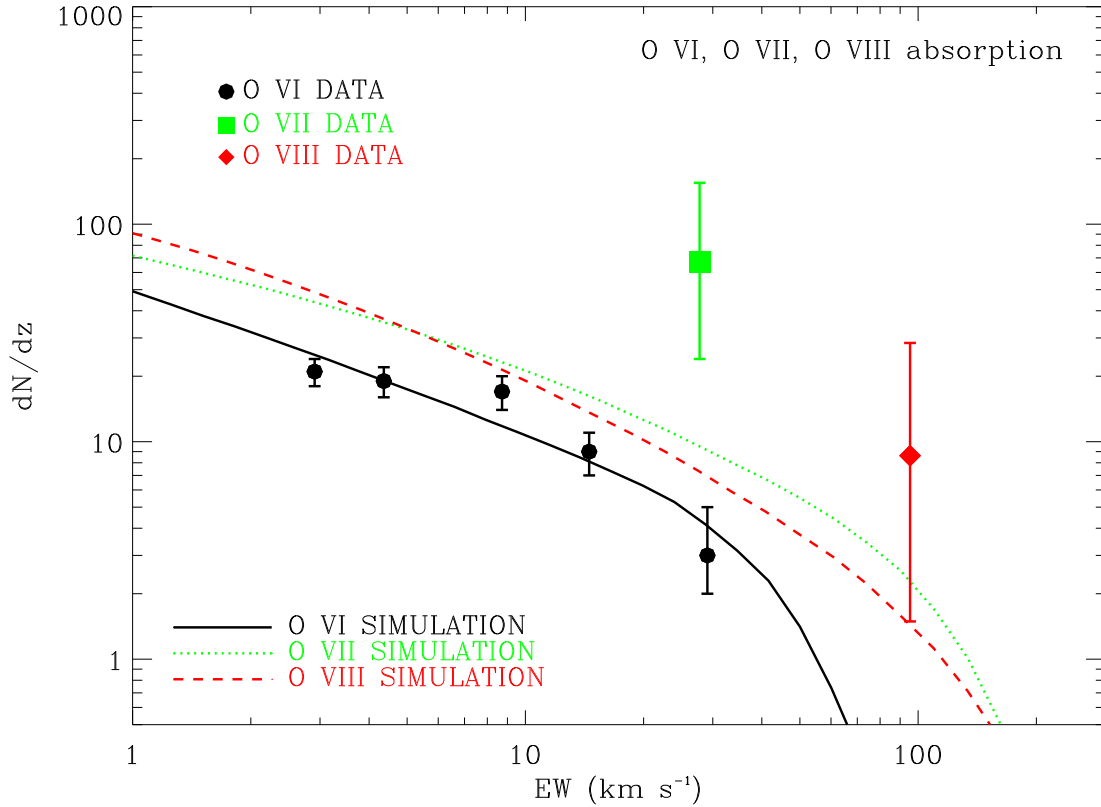


Fig. 5.— shows the number of all three absorption lines, O VI (solid), O VII (dotted) and O VIII (dashed), per unit redshift as a function of equivalent width in units of km/s, from the simulation with GSW. The symbols are observations by Danforth & Shull (2005), Nicastro et al. (2005) and Fang et al. (2005) for O VI, O VII and O VIII absorption lines, respectively.

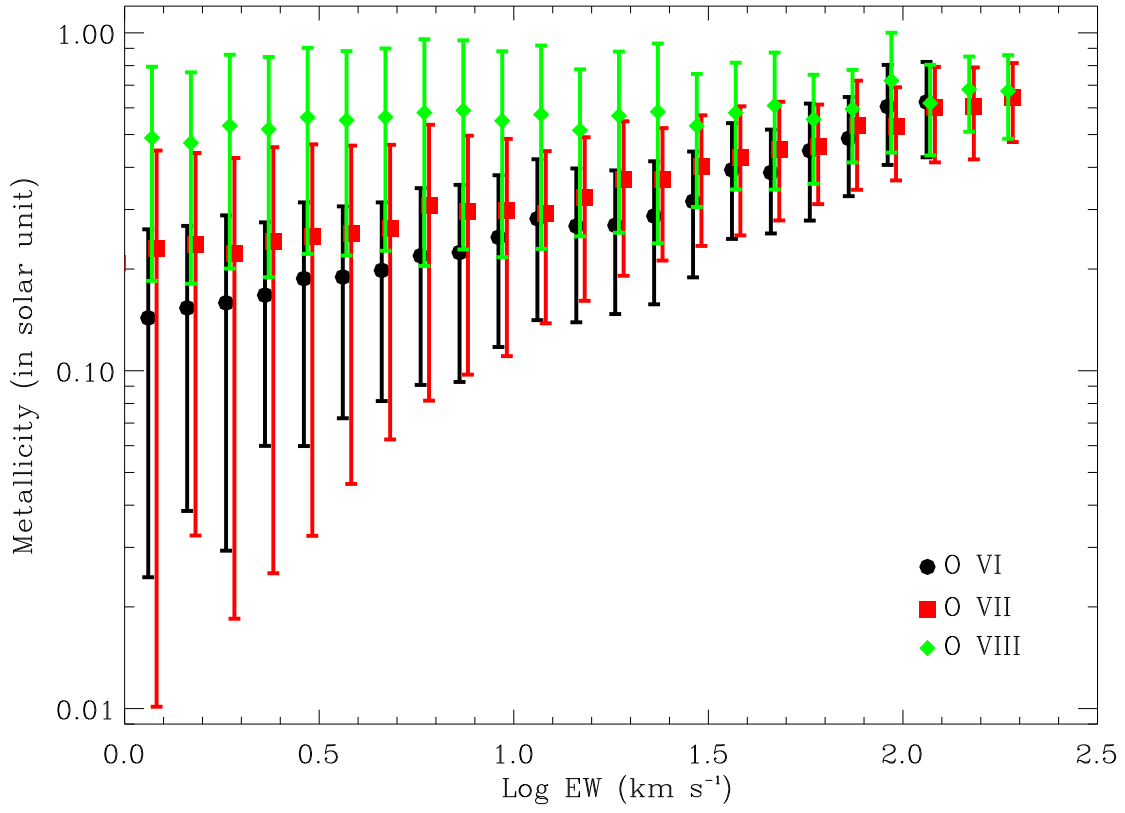


Fig. 6.— shows the average metallicity of O VI, O VI, O VIII absorption lines as a function of equivalent widths. The errorbars indicate the scatter about the average.

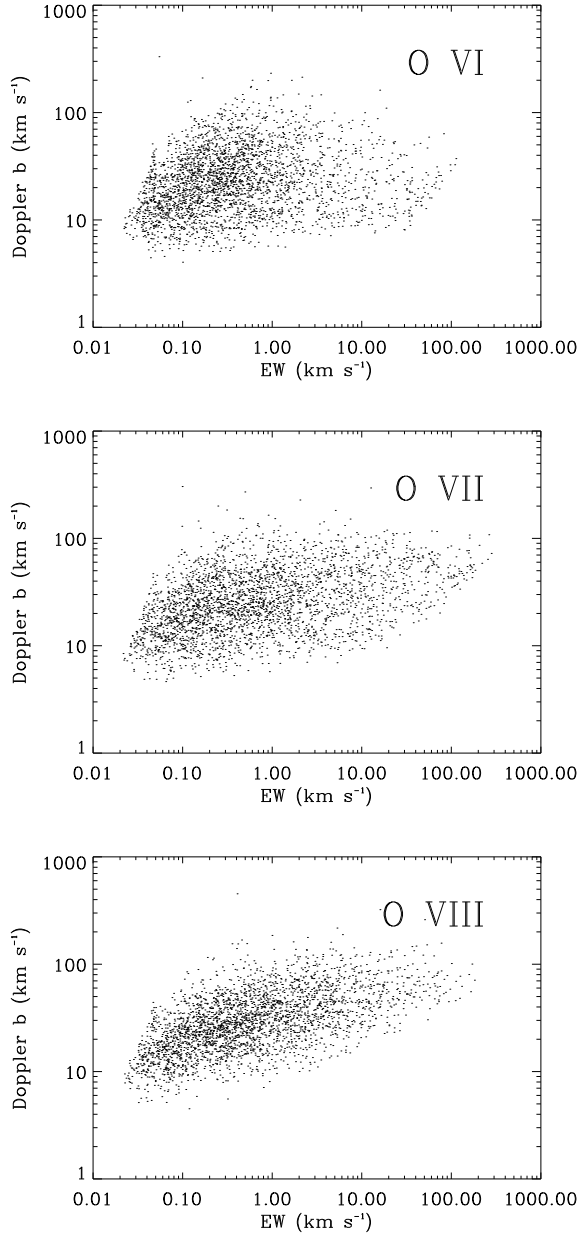


Fig. 7.— shows the b-parameter of lines versus their equivalent widths, for O VI (top), O VII (middle) and O VIII (bottom panel).

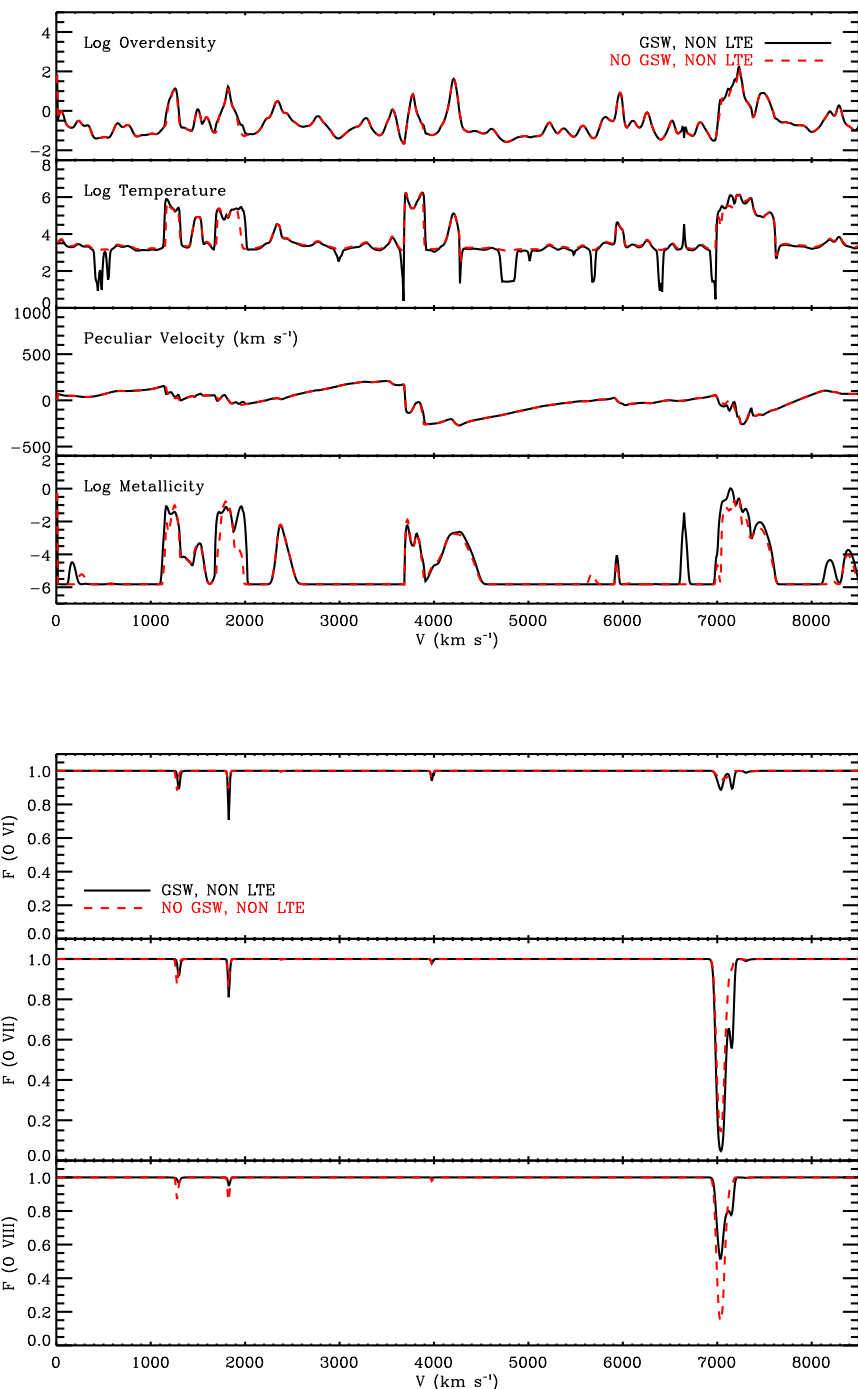


Fig. 8.— shows one line of sight through the simulation box. The top four panels from top to bottom give gas overdensity, temperature, peculiar velocity and metallicity (in solar units), respectively. The bottom three panels from top to bottom are flux absorption spectra for O VI, O VII and O VIII lines, respectively. The solid curves are for the simulation with GSW and the dashed curves without GSW.

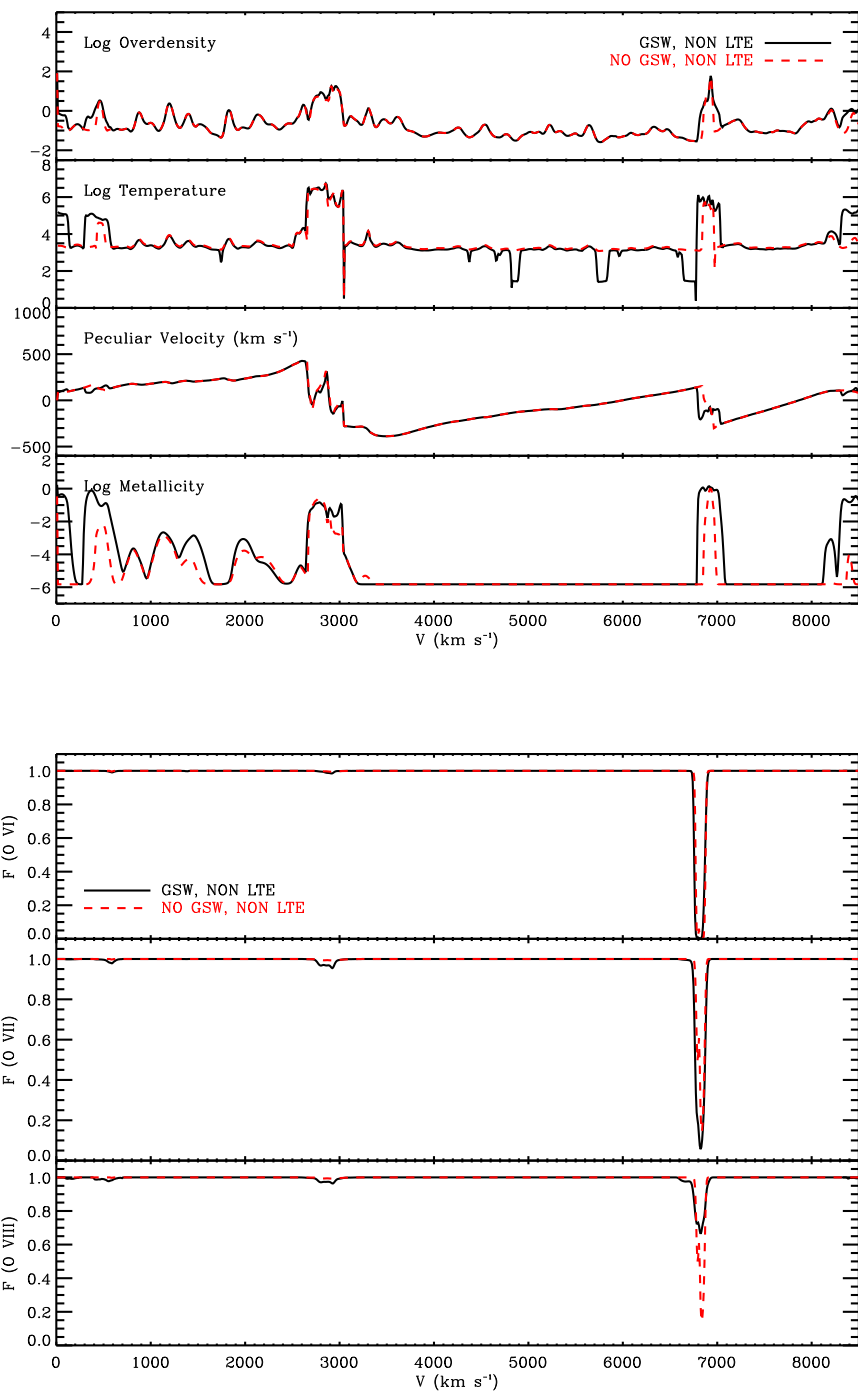


Fig. 9.— shows another line of sight through the simulation box. The top four panels from top to bottom give gas overdensity, temperature, peculiar velocity and metallicity (in solar units), respectively. The bottom three panels from top to bottom are flux absorption spectra for O VI, O VII and O VIII lines, respectively. The solid curves are for the simulation with GSW and the dashed curves without GSW.

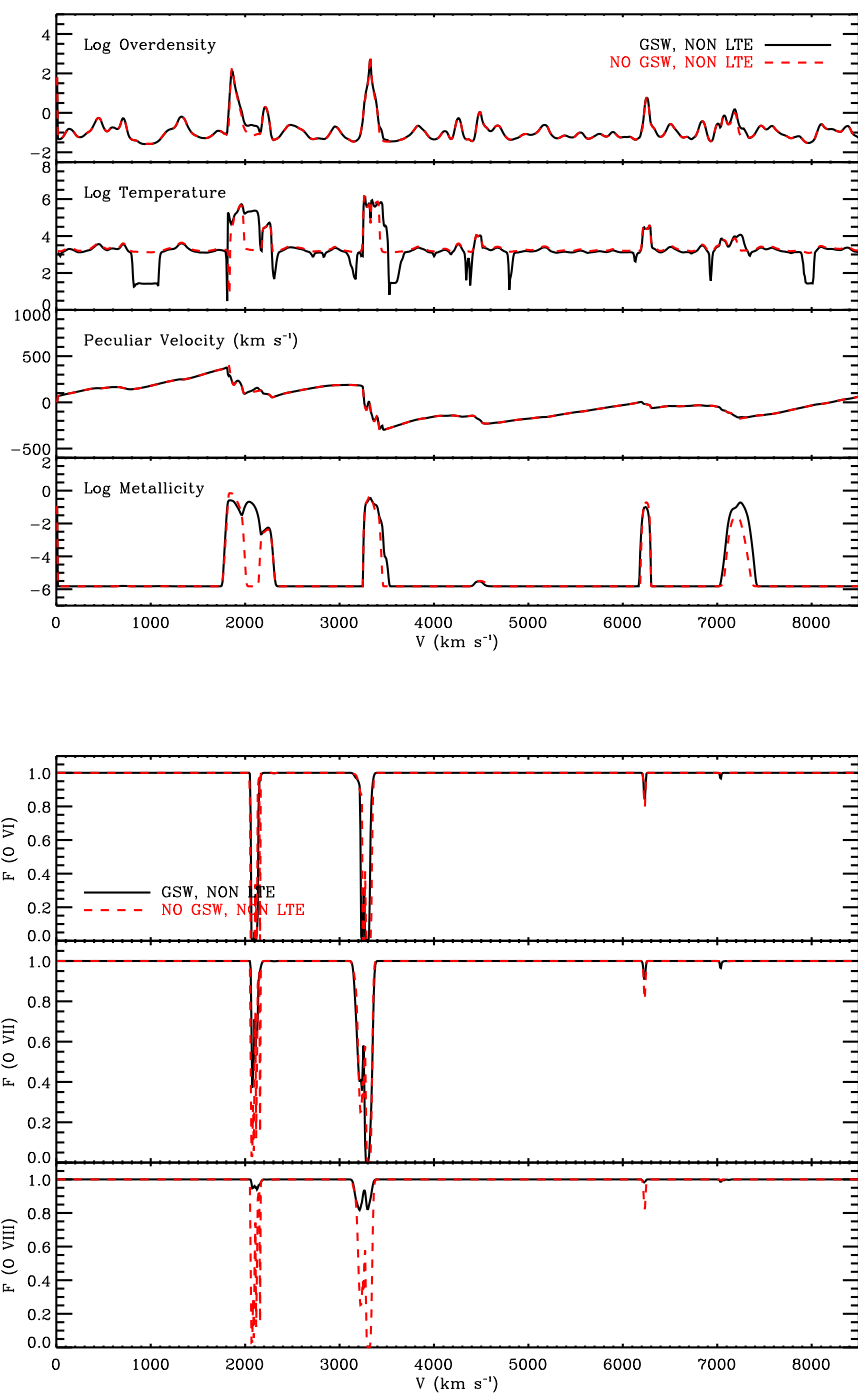


Fig. 10.— shows another line of sight through the simulation box. The top four panels from top to bottom give gas overdensity, temperature, peculiar velocity and metallicity (in solar units), respectively. The bottom three panels from top to bottom are flux absorption spectra for O VI, O VII and O VIII lines, respectively. The solid curves are for the simulation with GSW and the dashed curves without GSW.

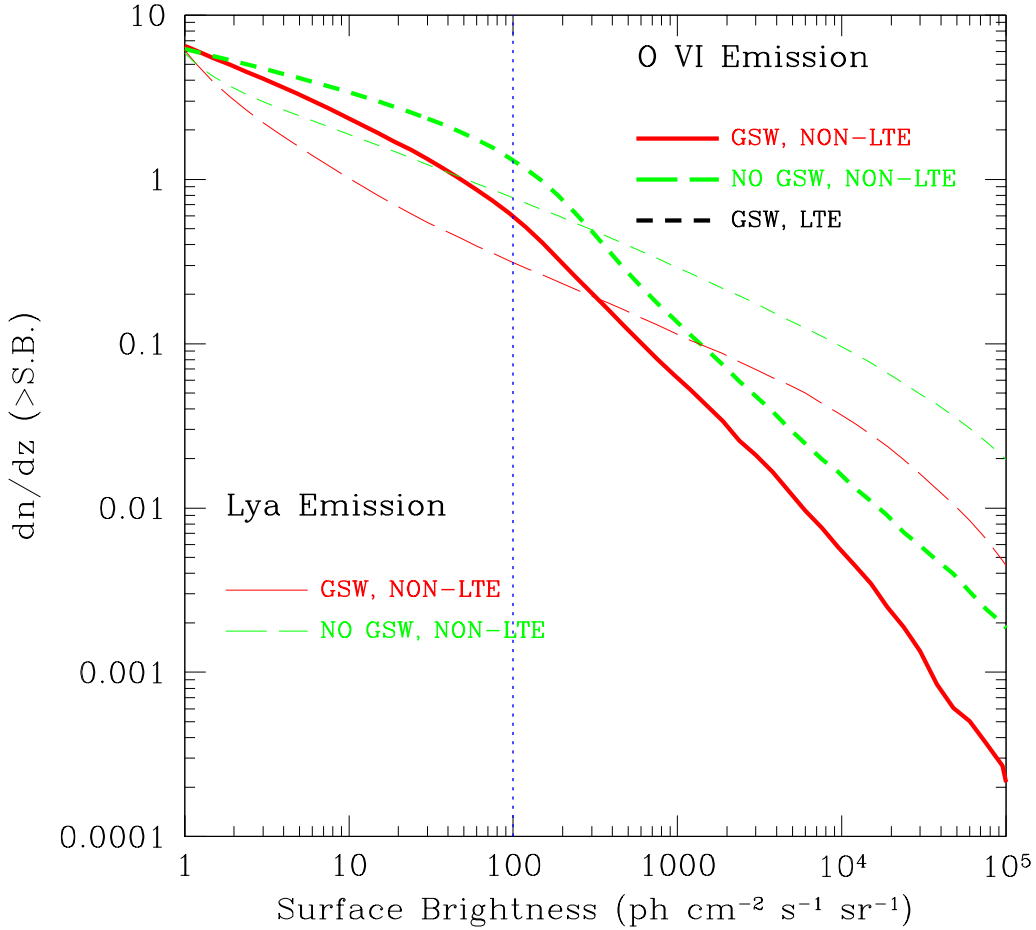


Fig. 11.— shows the cumulative number of O VI (thick curves) and Ly α lines (thin curves) per unit redshift as a function of surface brightness. The red curves show results from the simulation with GSW and the green curve from the simulation without GSW. The black curve (for O VI line only) is computed using CLOUDY code on the assumption of ionization equilibrium based on the density, temperature and metallicity information from the simulation with GSW. Note that future planned UV missions may be able to achieve a sensitivity in the range 100 in the displayed units, as indicated by the vertical blue line.

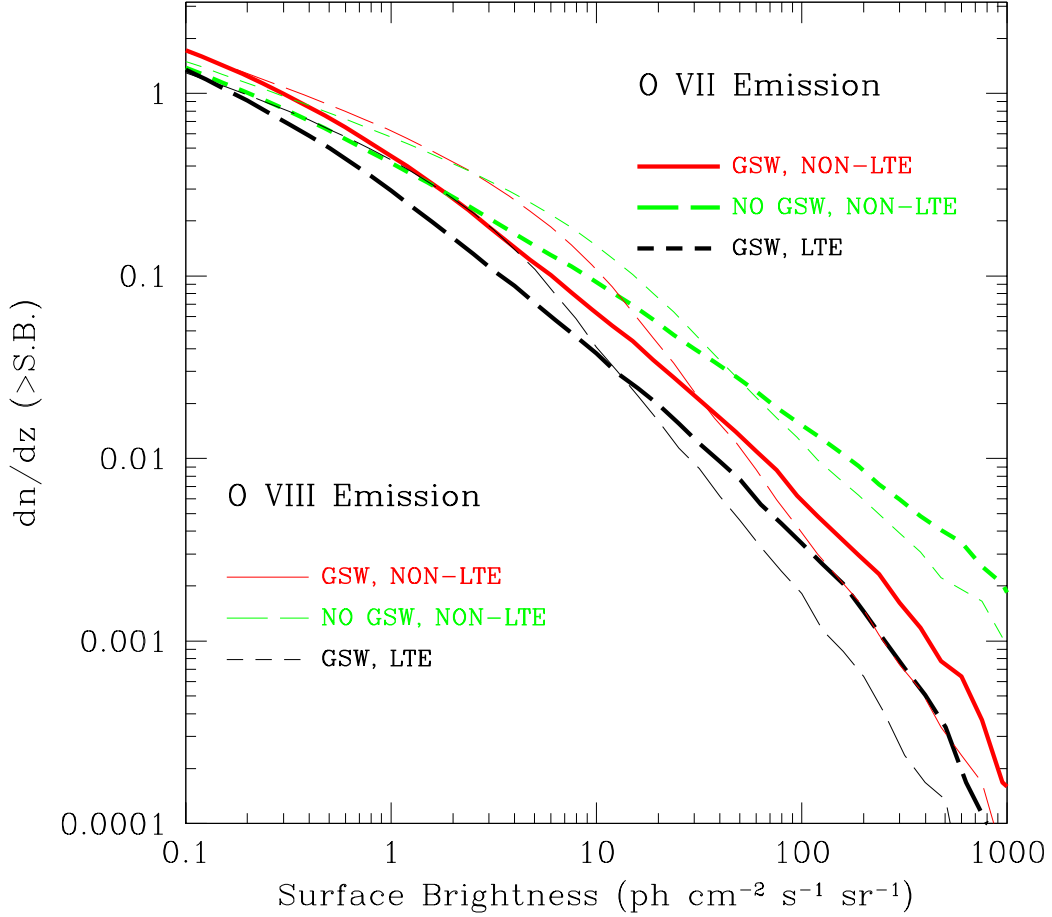


Fig. 12.— shows the cumulative number of O VII (thick curves) and O VIII lines (thin curves) per unit redshift as a function of surface brightness. The red curves show results from the simulation with GSW and the blue curve from the simulation without GSW. The green curve is computed using CLOUDY code on the assumption of ionization equilibrium based on the density, temperature and metallicity information from the simulation with GSW. The planned Japanese soft X-ray emission DIOS (Yoshikawa et al. 2003) will have a sensitivity of order 0.1 in the displayed units.

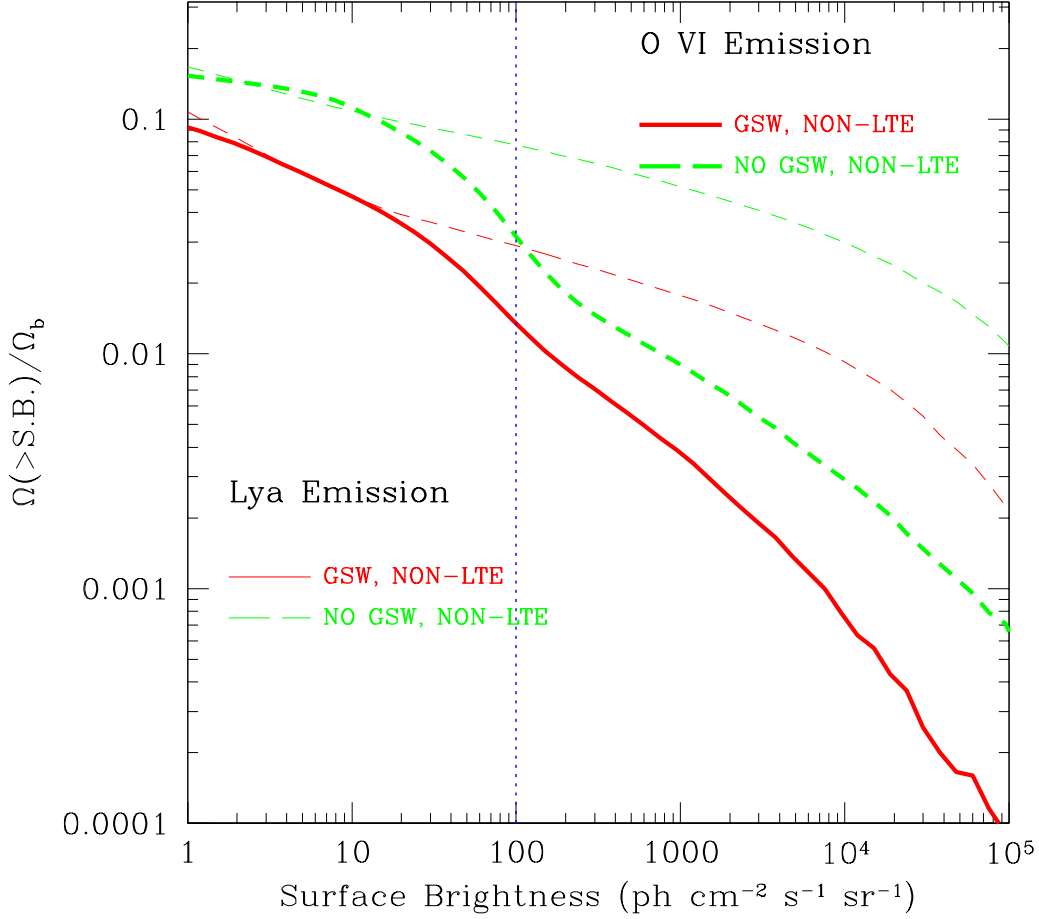


Fig. 13.— shows the cumulative gas mass density probed by the O VI (thick curves) and Ly α (thin curves) lines as a function of surface brightness. The red curves show results from the simulation with GSW and the green curves from the simulation without GSW.

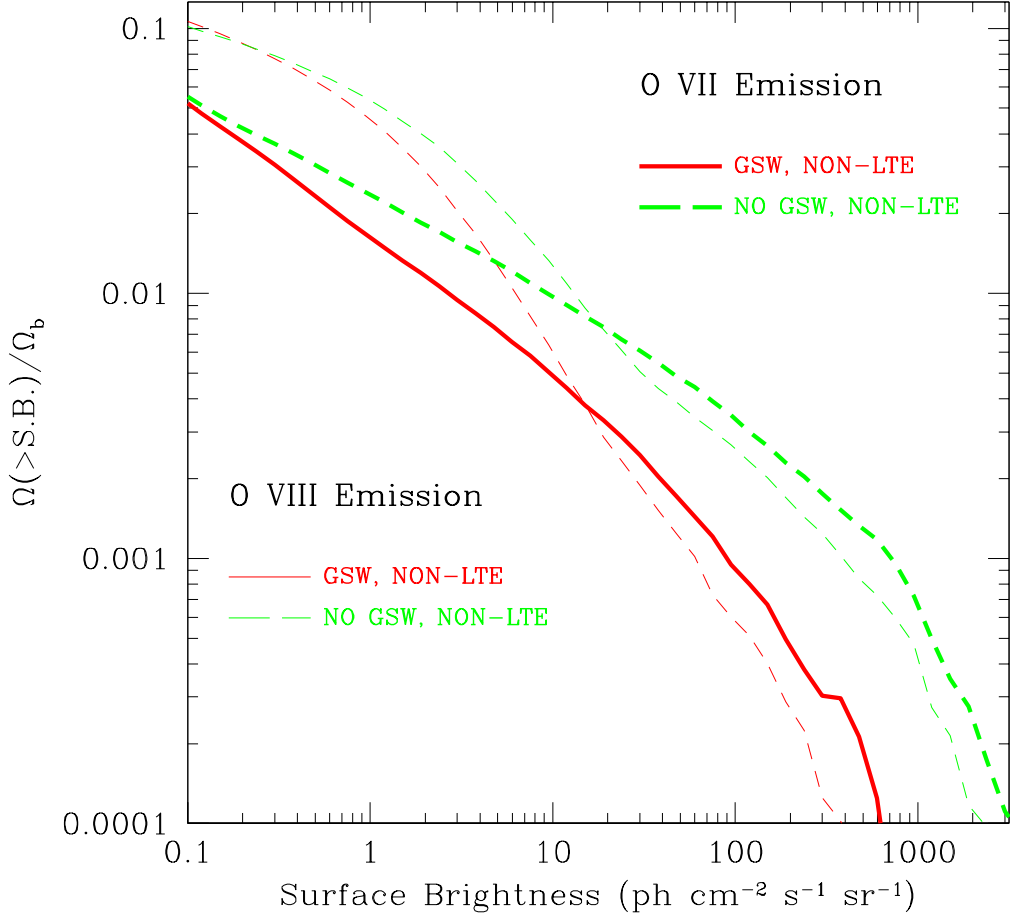


Fig. 14.— shows the cumulative gas mass density probed by the O VII (thick curves) and O VIII (thin curves) lines as a function of surface brightness. The red curves show results from the simulation with GSW and the green curves from the simulation without GSW.

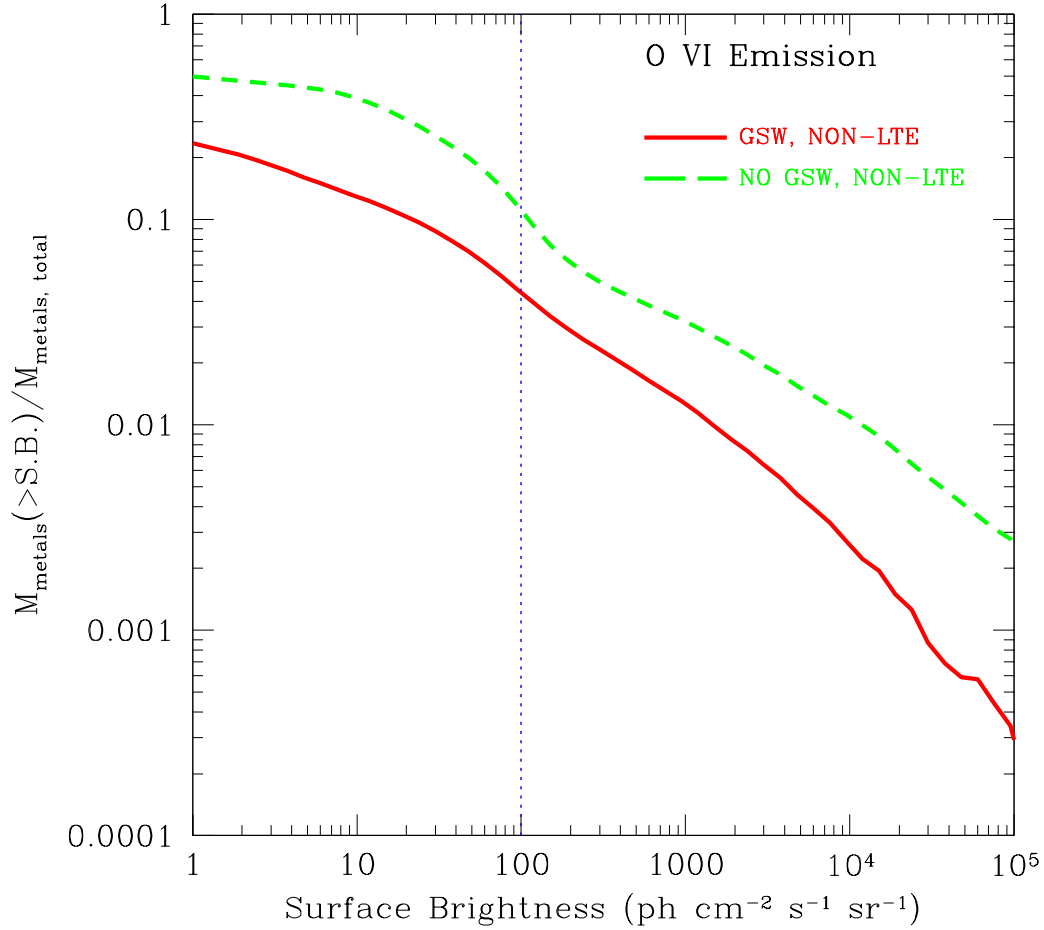


Fig. 15.— shows the cumulative metal mass probed by the O VI line as a function of surface brightness. The red curves show results from the simulation with GSW and the green curves from the simulation without GSW.

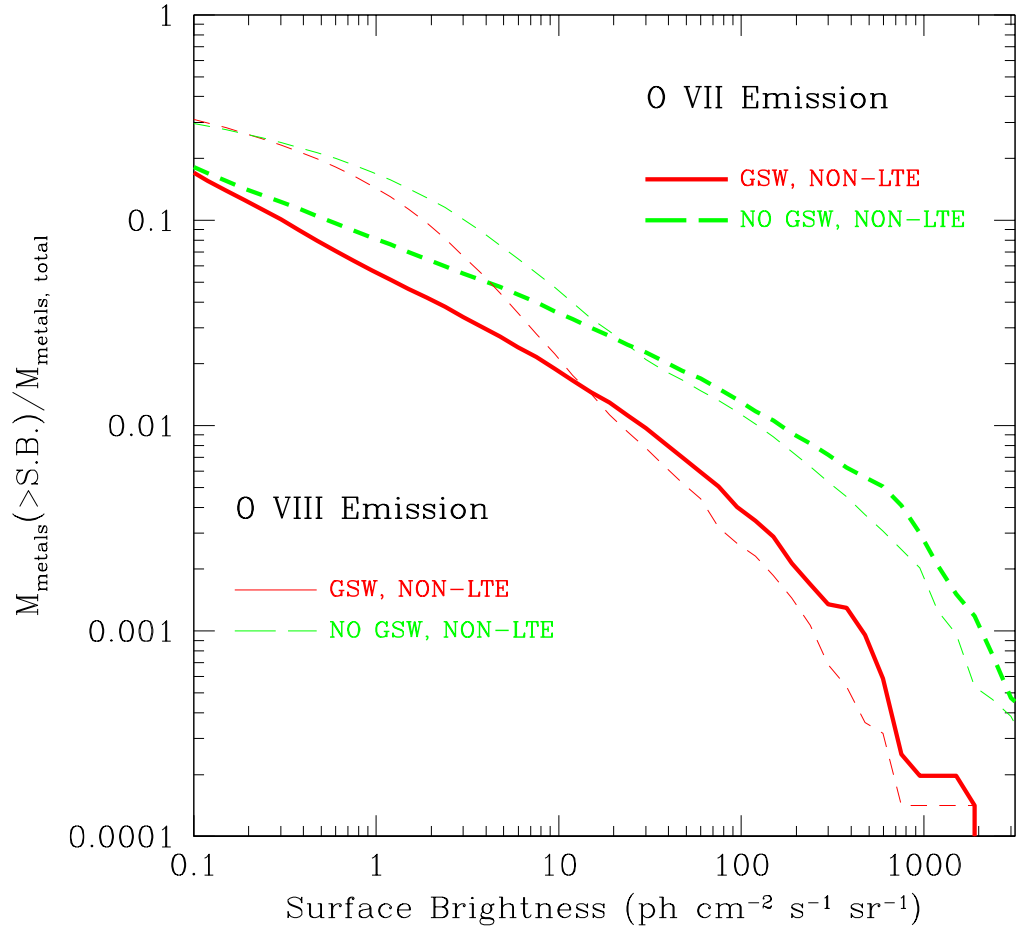


Fig. 16.— shows the cumulative metal mass probed by the O VII (thick curves) and O VIII (thin curves) lines as a function of surface brightness. The red curves show results from the simulation with GSW and the green curves from the simulation without GSW.

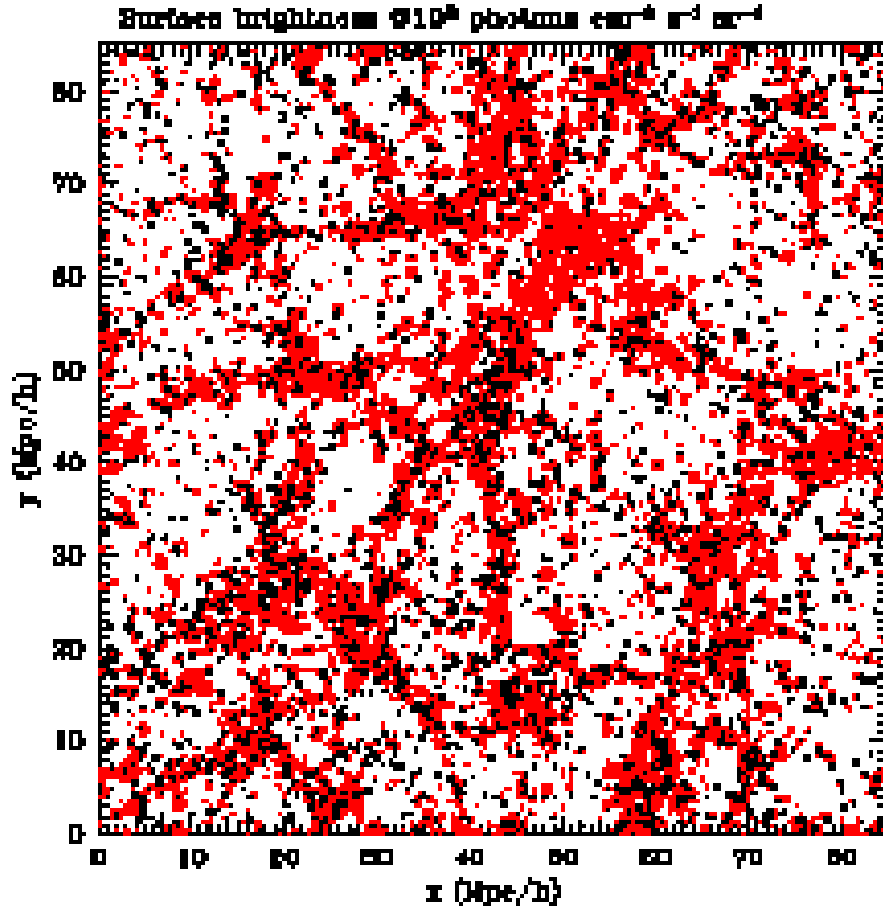


Fig. 17.— shows a map of size $85 \times 85 \text{Mpc}^2/h^2$ with a depth of $85 \text{Mpc}/h$, with the observable regions shown as black spots for O VI emission line with an instrument of a sensitivity of $100 \text{ photon cm}^{-2} \text{sr}^{-1} \text{s}^{-1}$. The red contours are the underlying gas density distribution.

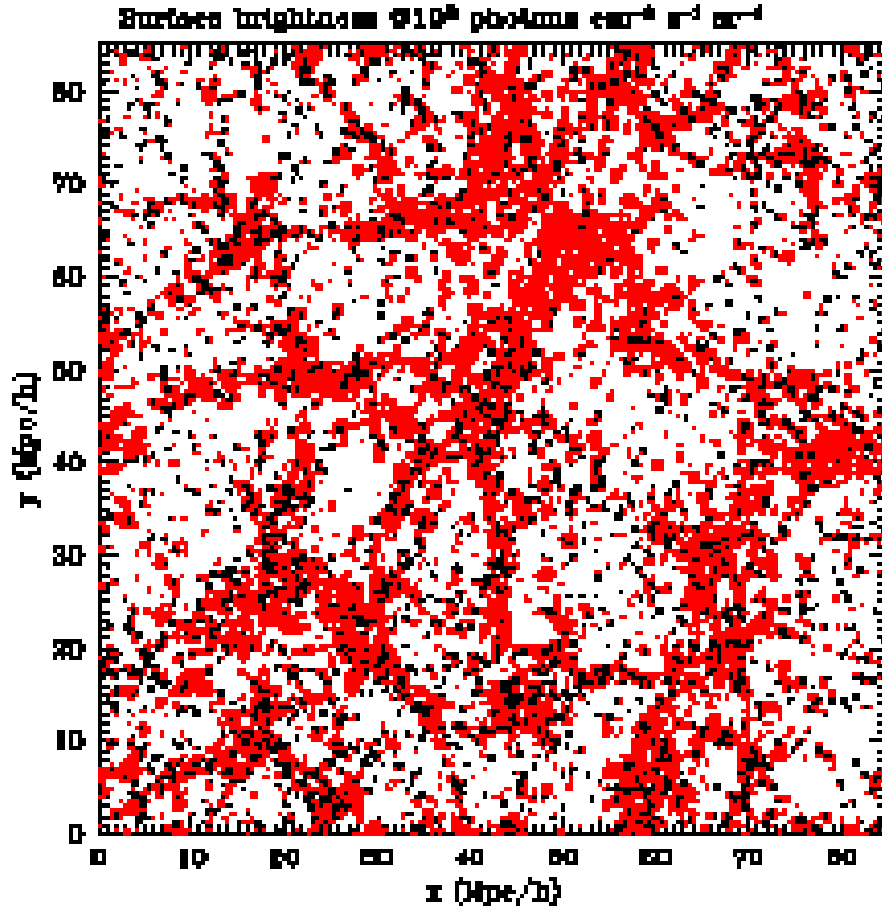


Fig. 18.— shows a map of size $85 \times 85 \text{Mpc}^2/h^2$ with a depth of $85 \text{Mpc}/h$, with the observable regions shown as black spots for Ly α emission line with an instrument of a sensitivity of $100 \text{ photon cm}^{-2} \text{sr}^{-1} \text{s}^{-1}$. The red contours are the underlying gas density distribution.

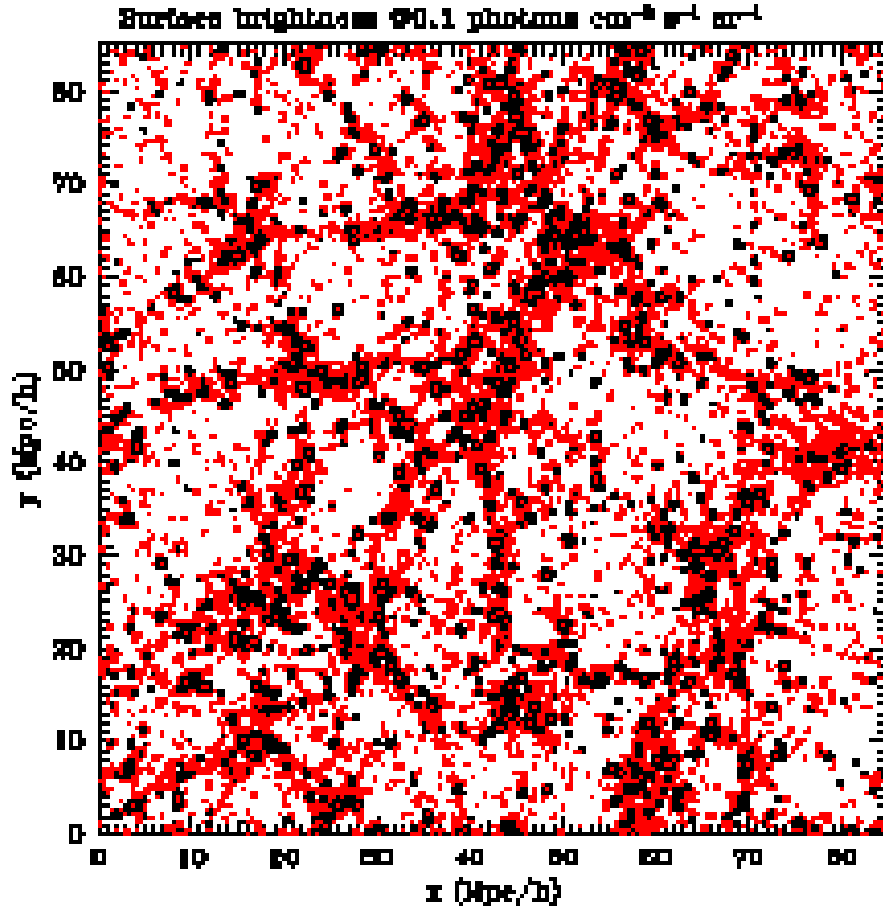


Fig. 19.— shows a map of size $85 \times 85 \text{Mpc}^2/h^2$ with a depth of $85 \text{Mpc}/h$, with the observable regions shown as black spots for O VII emission line with an instrument of a sensitivity of $0.1 \text{ photon cm}^{-2} \text{sr}^{-1} \text{s}^{-1}$. The red contours are the underlying gas density distribution.

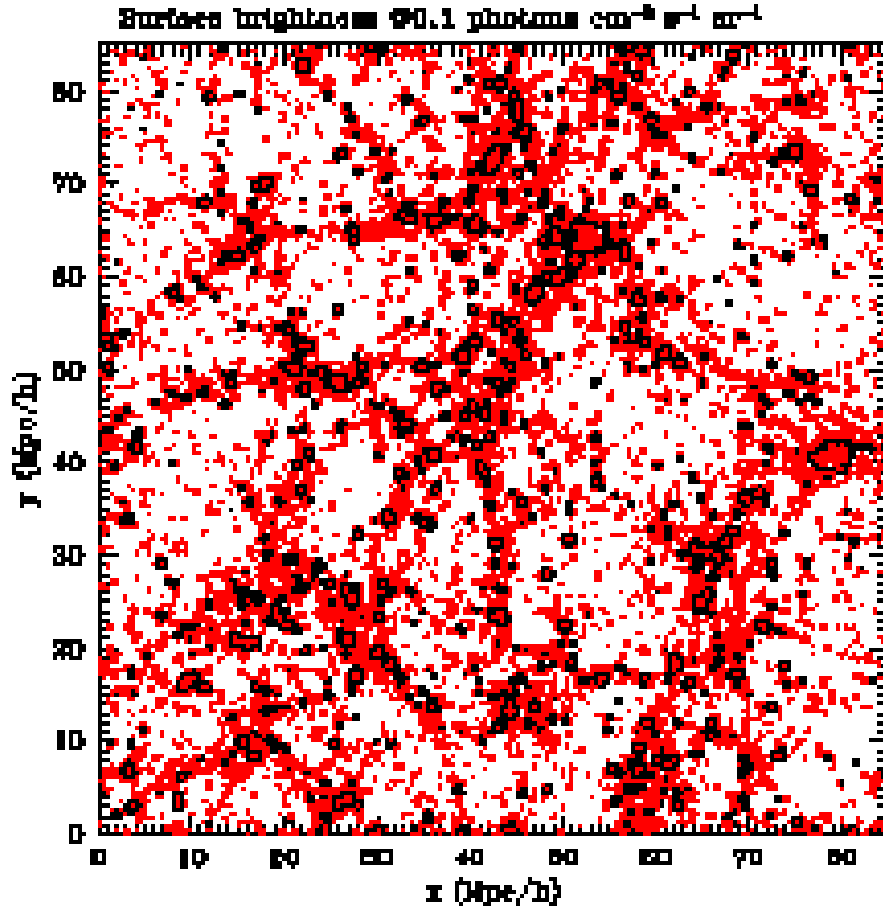


Fig. 20.— shows a map of size $85 \times 85 \text{Mpc}^2/h^2$ with a depth of $85 \text{Mpc}/h$, with the observable regions shown as black spots for O VIII emission line with an instrument of a sensitivity of $0.1 \text{ photon cm}^{-2} \text{sr}^{-1} \text{s}^{-1}$. The red contours are the underlying gas density distribution.

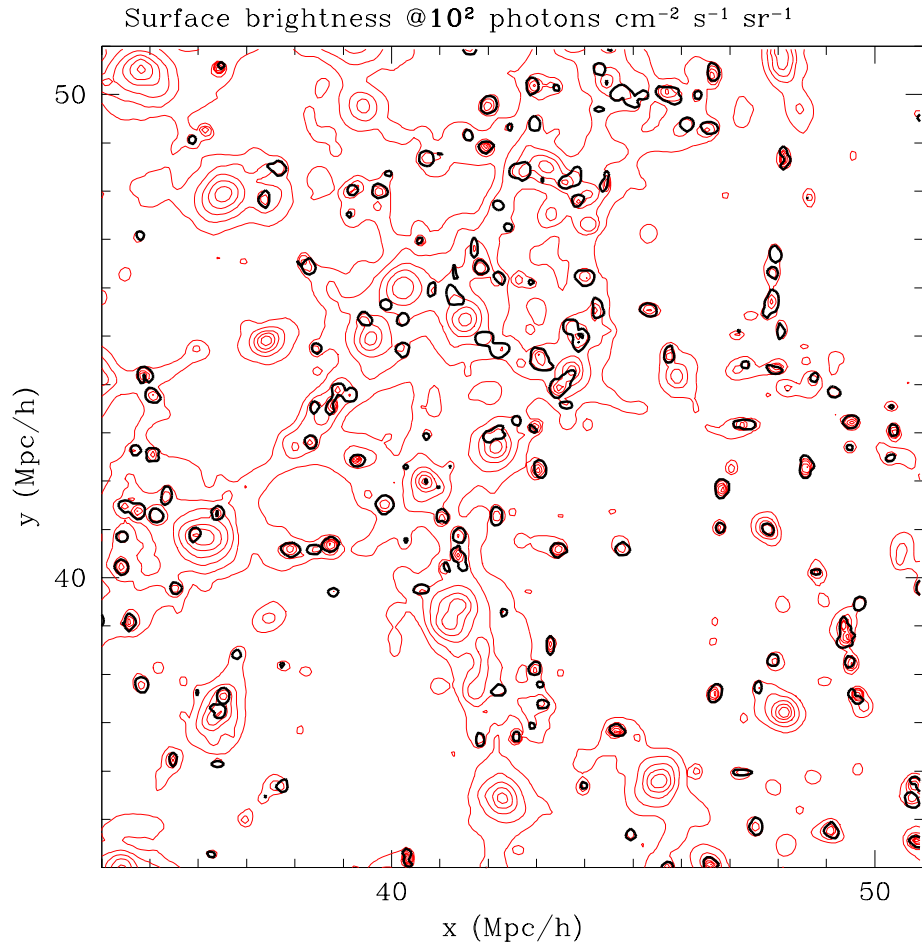


Fig. 21.— shows a part of Figure 17 by zooming into a small region to better display some details, showing the observable regions shown as black spots with O VI emission line with an instrument of a sensitivity of $100 \text{ photon cm}^{-2} \text{sr}^{-1} \text{s}^{-1}$. The red contours are the underlying gas density distribution.

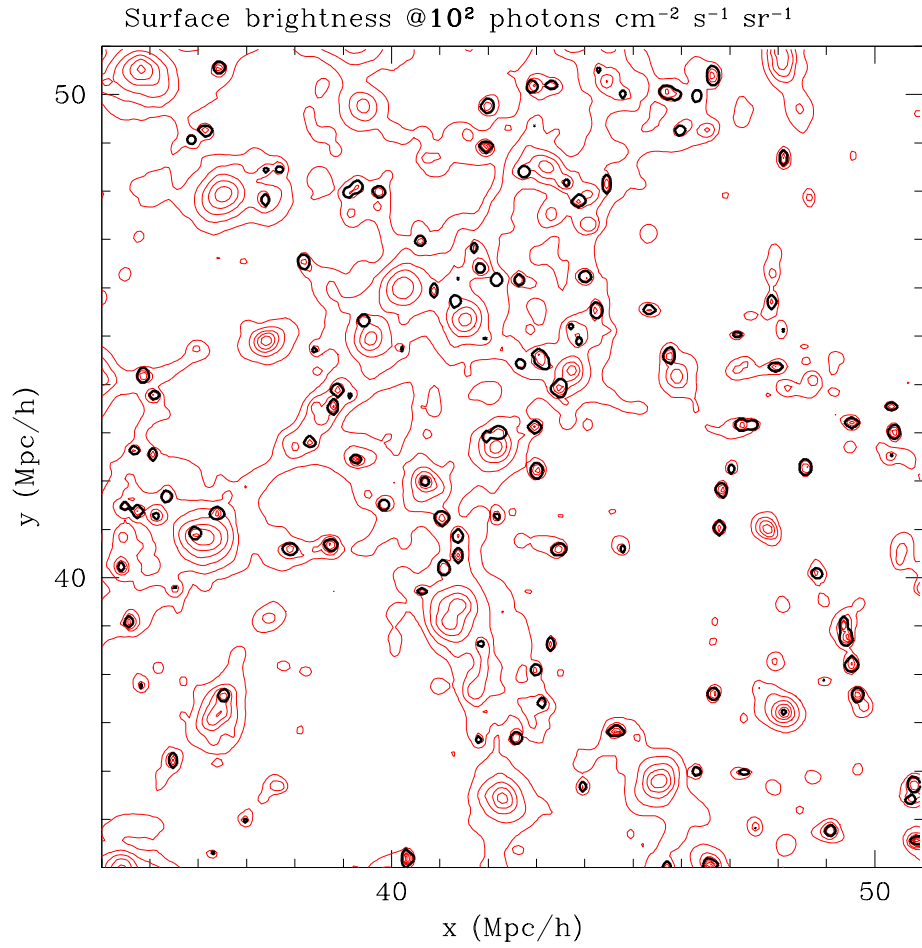


Fig. 22.— shows a part of Figure 18 by zooming into a small region to better display some details, showing the observable regions shown as black spots with Ly α emission line with an instrument of a sensitivity of $100 \text{ photon cm}^{-2} \text{sr}^{-1} \text{s}^{-1}$. The red contours are the underlying gas density distribution.

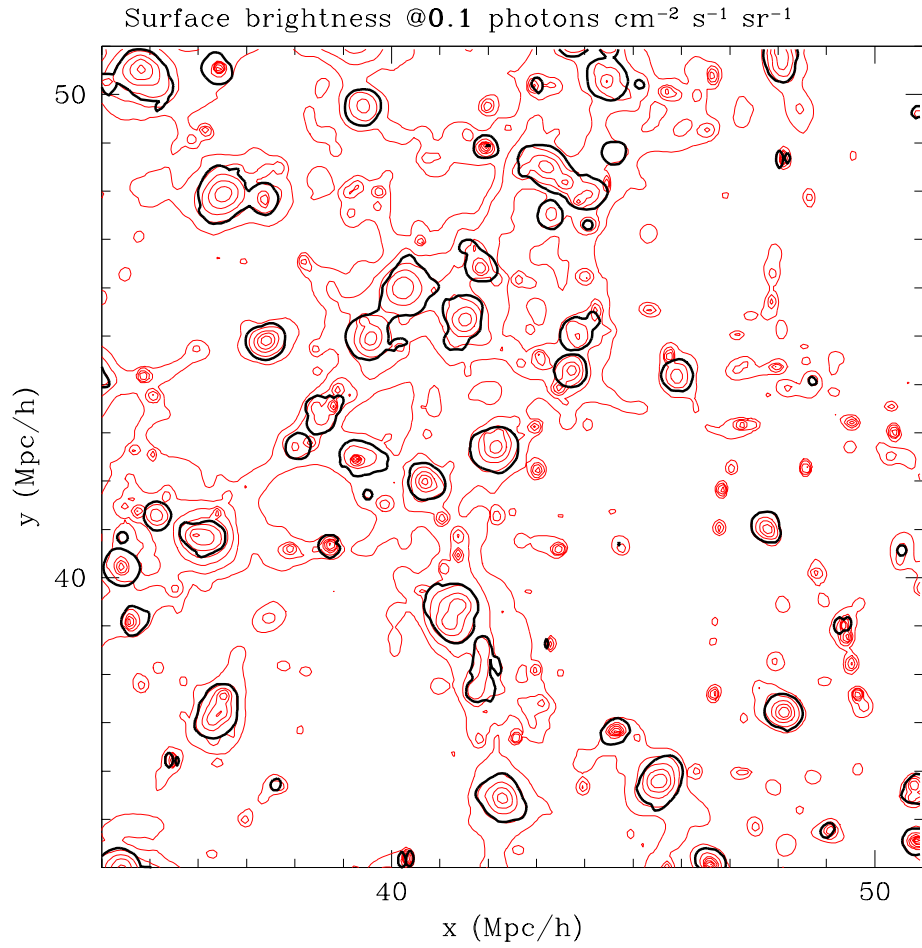


Fig. 23.— shows a part of Figure 19 by zooming into a small region to better display some details, showing the observable regions shown as black spots with O VII emission line with an instrument of a sensitivity of $0.1 \text{ photon cm}^{-2} \text{sr}^{-1} \text{s}^{-1}$. The red contours are the underlying gas density distribution.

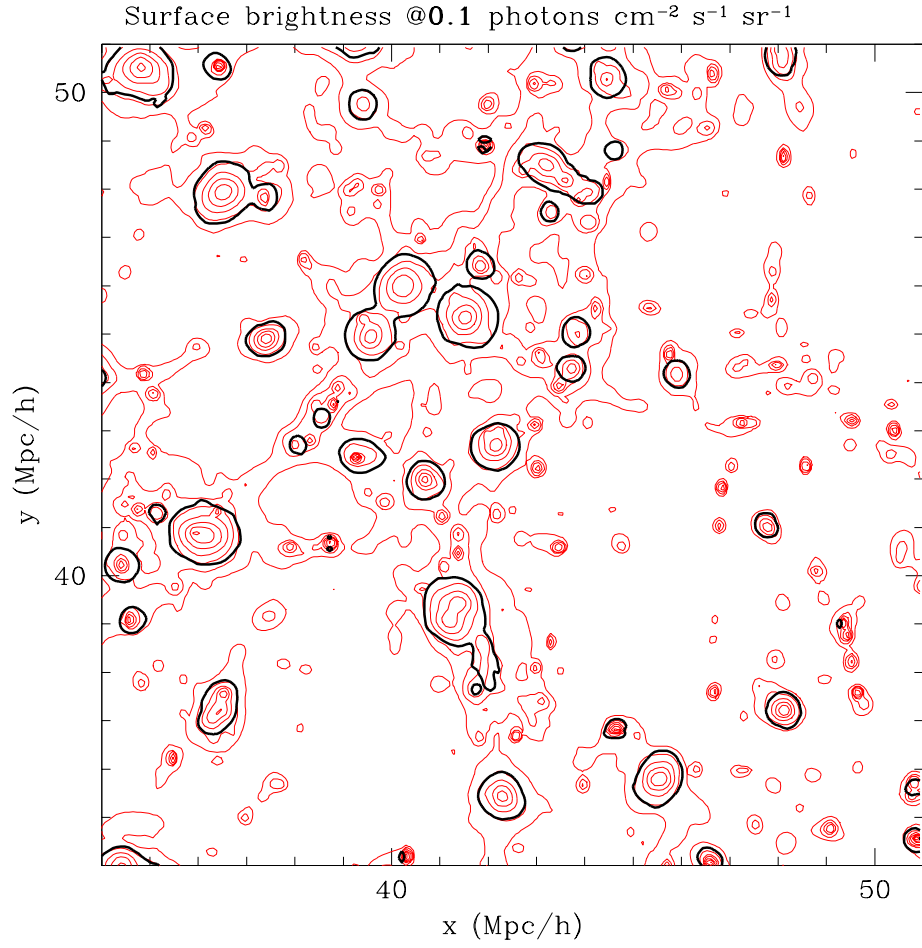


Fig. 24.— shows a part of Figure 20 by zooming into a small region to better display some details, showing the observable regions shown as black spots with O VIII emission line with an instrument of a sensitivity of $0.1 \text{ photon cm}^{-2} \text{sr}^{-1} \text{s}^{-1}$. The red contours are the underlying gas density distribution.

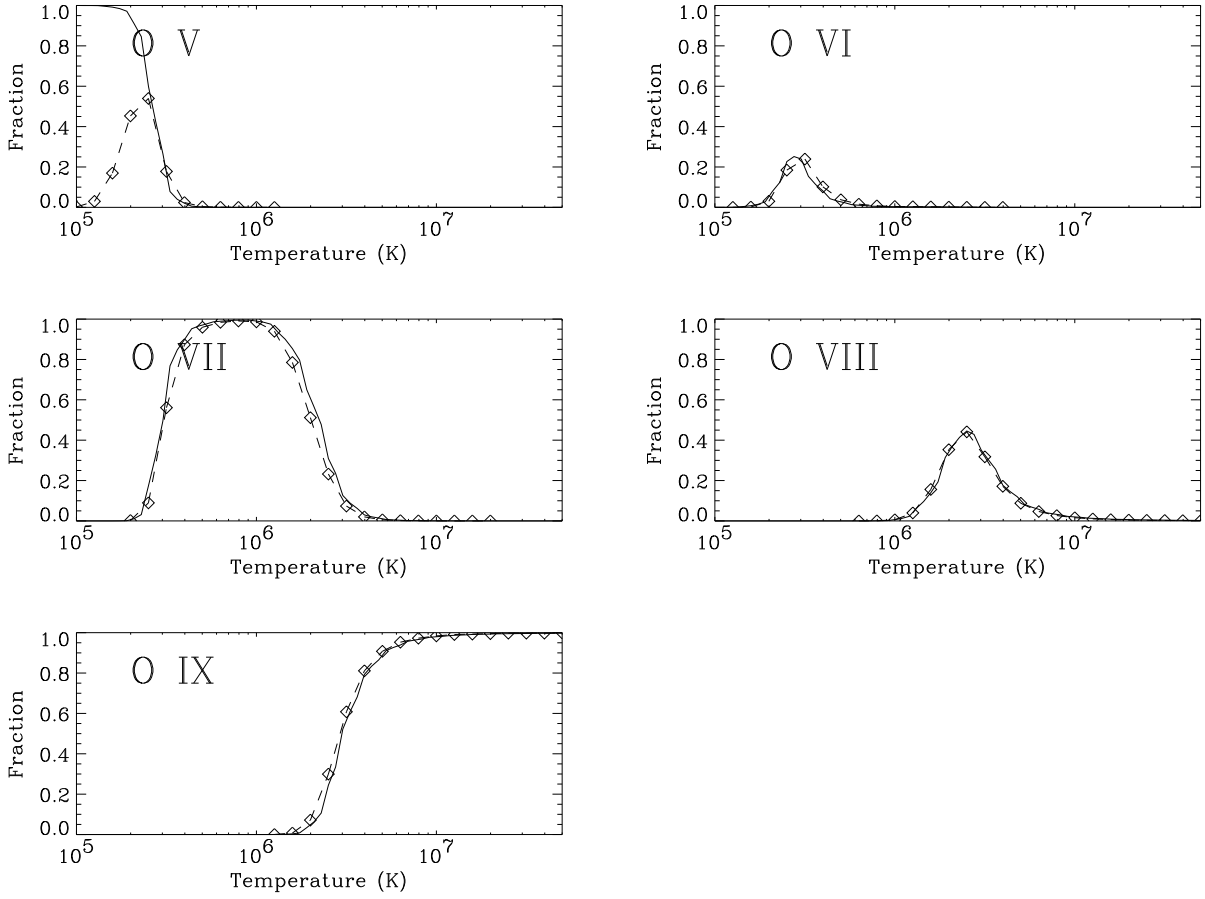


Fig. 25.— shows the comparison between our calculation with very long integration time and equilibrium calculation for the collisional ionization case with zero background radiation field. The solid lines in each panel are results from our calculation, and the diamonds are adopted from Mazzotta et al. (1998), based on collisional ionization equilibrium.

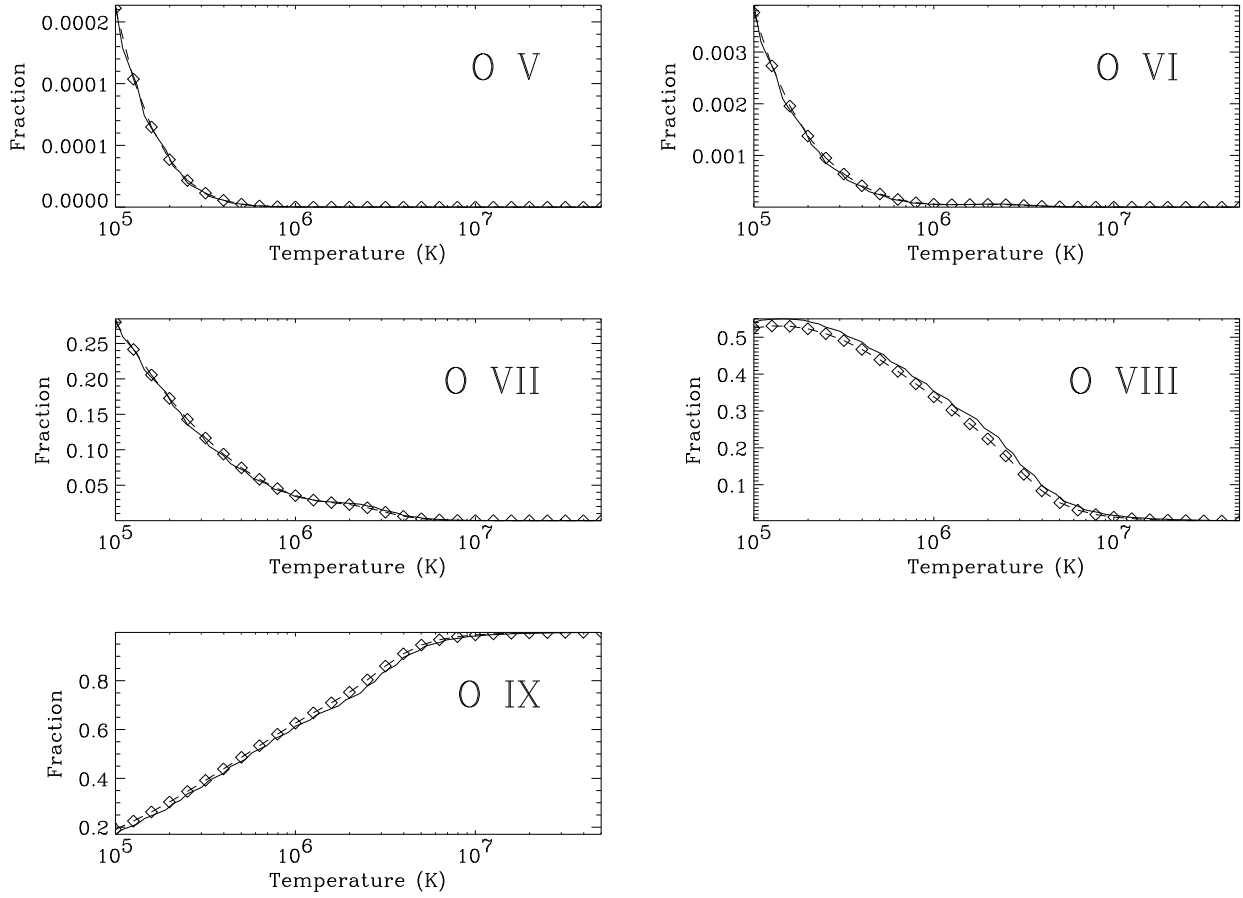


Fig. 26.— a similar comparison between our calculation as in Figure 25, with an addition of a background radiation field of $J(912\text{\AA}) = 10^{-22} \text{ ergs s}^{-1}\text{cm}^{-2}\text{Hz}^{-1}\text{sr}^{-1}$.

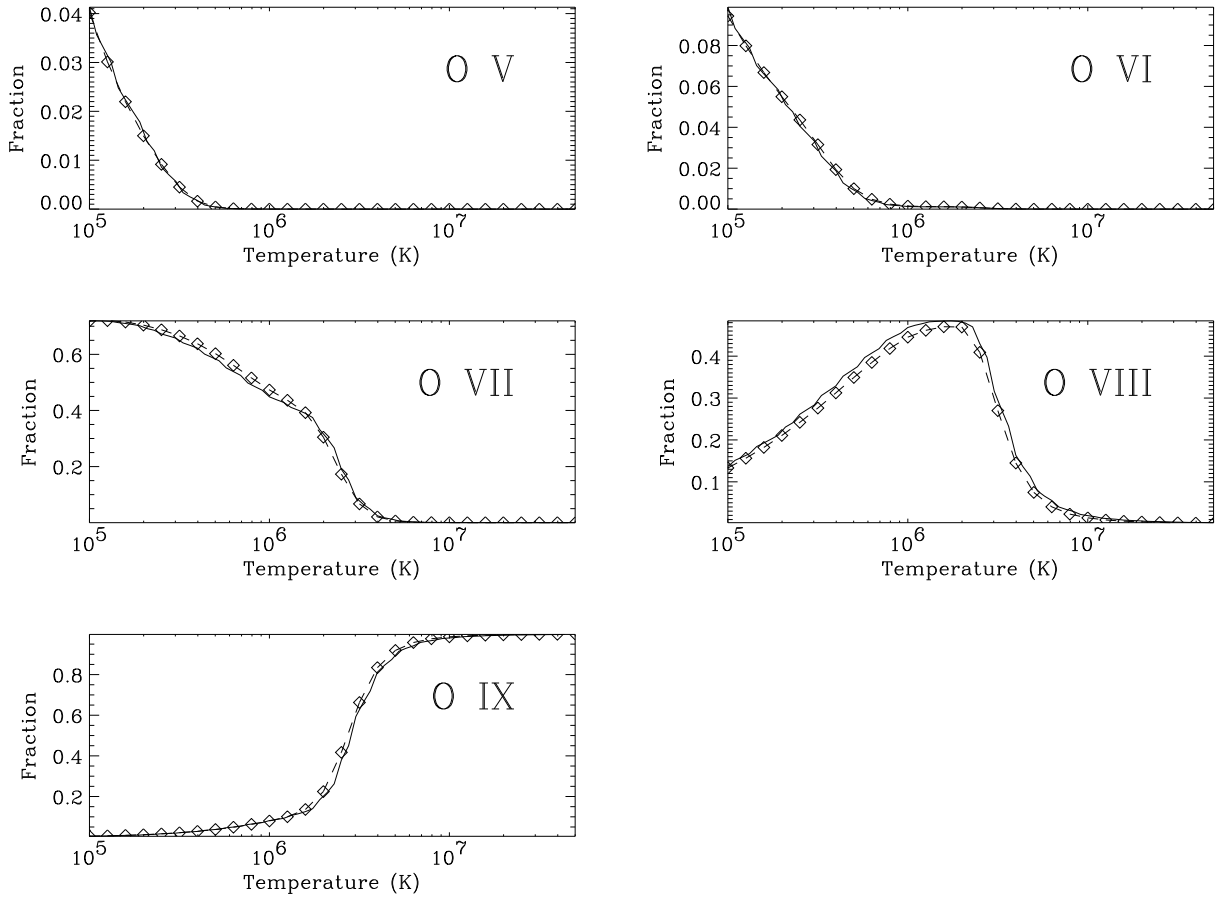


Fig. 27.— a similar comparison between our calculation as in Figure 25, with a different background radiation field of $J(912\text{\AA}) = 10^{-23}$ ergs s $^{-1}$ cm $^{-2}$ Hz $^{-1}$ sr $^{-1}$.